Short Papers

Numerical Analysis of Complicated Waveguide Circuits on the Basis of Generalized Scattering Matrices and Domain Product Technique

Vitaliy P. Chumachenko and Vladimir P. Pyankov

***Abstract*—H- and E-plane waveguide structures having arbitrarily polygonal boundaries and piecewise homogeneous fillings are considered in this paper. A modified version of the generalized scattering matrix (S-matrix) method is applied to their analysis. More specifically, the segmentation of the whole unit is carried out. A homogeneously filled multiangular region, supplied with flanged apertures, is taken as a key building block. Scattering matrix of the block consists of amplitudes of elliptic waves propagating from the apertures in the corresponding half-spaces. Evaluation of the S-matrix is based on the domain product technique (DPT). Numerical examples demonstrating the efficiency, flexibility, and reliability of the approach are also presented.**

***Index Terms*—Domain product technique, scattering matrix, waveguide components, waveguide discontinuities.**

I. Introduction

The simulation of the H- and E-plane waveguide structures has numerous applications in microwave circuit design. The literature on this subject is very extensive. Of many books and papers, we mention only [1]–[8] discussing the problem and giving references.

A conventional approach to the analysis of a complex structure consists of dividing the whole unit into building blocks and subsequently exploiting the method of generalized scattering (or other circuit) matrices [1]–[3], [7]. Here, for obtaining the characteristics of the entire multielement object with the required accuracy, S-matrices of the separate parts are to be determined with a high precision, owing to possible accumulation of calculation errors. The approach works successfully if the suitable building blocks emerge after segmentation, which can be studied on the basis of effective numerical analytical techniques such as, e.g., the modified residual technique [1] or semiinversion method [8]. The set of such objects is clearly limited in number. Direct numerical or hybrid methods (the latter ones include the first as components) are used for the analysis of more complicated structures. Direct numerical methods are more versatile, but require a large computer memory and longer computing time. Their computational efficiency can noticeably decrease in the presence of edges on the scatterer contour, especially in finding amplitudes of higher order modes [8].

In this paper, we propose to replenish the set of key building blocks with a new one. A very flexible unit is constructed in such a manner that its characteristics can be accurately found based on the domain product technique (DPT) [9]. The above configuration is similar to the one used in recently published work [10] analyzing scattering from the groove in a ground plane. The interior part of the block (result of segmentation) is a homogeneously filled region bounded by arbitrary polygon. The boundary has "windows" supplied with infinite planar flanges. The S-matrix of the block consists of amplitudes of elliptic waves propagating in the corresponding half-spaces from the flanged apertures. Regular waveguides are attached to the irregular part of the junction by introducing a block having the form of the open-ended waveguide with the flange. Implementation of the S-matrix method based on the blocks proposed enables accurate analysis of the fairly complicated structures with low computational cost.

Manuscript received September 15, 1997.

V. P. Chumachenko is with Electronics Engineering Department, Gebze Institute of Technology, Gebze, Kocaeli, Turkey, on leave from the Technical University of Zaporizhzhya, Zaporizhzhya 330063, Ukraine.

V. P. Pyankov is with the Department of Higher Mathematics, Technical University of Zaporizhzhya, Zaporizhzhya 330063, Ukraine.

Publisher Item Identifier S 0018-9480(00)00842-5.

II. Formulation

Geometry of the problem is shown in Fig. 1(a). The modeled multilayer structure is uniform along the axis and has a size in this direction. It is an H- or E-plane waveguide junction filled by piecewise homogeneous lossless magnetodielectric. In further discussion, we shall distinguish between these cases as (H) and (E), respectively. Every medium may contain multiangular perfectly conducting inclusions having no contact with the interface. For the sake of simplicity, we assume that all the contours of their cross section are closed. The combined presence of ideal electric and magnetic walls is permissible. The last gives the possibility to reduce the order of simultaneous equations in the problem for symmetric geometry. We also consider the cross section of any part of interfaces as a single segment with the end points on the perfectly conducting boundaries. LM_{pl} (H) or LE_{pl} (E) modes are excited in the structure. Here, l is fixed and the same for different waveguides and denotes the number of the field variations along Oz. The time factor $\exp(i\varpi t)$ is omitted and suppressed throughout. Z-dependence $\cos(l\pi z/b)$ (H) or $\sin(l\pi z/b)$ (E) or $(H, E, b=\infty)$ in the field expressions is also omitted.

The problem is to find z-component U of electric (H) or magnetic (E) field satisfying the Helmholtz equation and the homogeneous Dirichlet (H) or Neumann (E) conditions on the conducting parts of the boundary. Those are taken in the reverse order on the magnetic walls. The conditions, which guarantee continuity of the tangential components of the field, are prescribed across the interfaces as

$$U_A = U_B \qquad \frac{\partial U_A}{\partial n} = P\frac{\partial U_B}{\partial n}. \tag{1}$$

Here, n is the normal to the perimeter

$$P = \frac{\varepsilon_B \cdot \chi_A^2}{\varepsilon_A \cdot \chi_B^2} \quad (H) \quad \text{or} \quad P = \frac{\mu_B \cdot \chi_A^2}{\mu_A \cdot \chi_B^2} \quad (E) \tag{2}$$

ε and μ are relative permittivity and permeability

$$\chi = 2\pi\sqrt{\frac{\varepsilon\mu}{\chi^2} - \left(\frac{l}{2b}\right)^2} \tag{3}$$

and λ is the free-space wavelength. The quantities are marked by indexes A and B on the opposite sides of the interface.

Let us disjoin the waveguide junction into the autonomous multiangular blocks with homogeneous fillings. In Fig. 1(b), they are shown separated by a finite distance d. The calculation formulas are obtained further for $d \to 0$. It is assumed that the apertures of the blocks and open-ended waveguides have infinite planar flanges superposing for $d = 0$. Quantities, related to an auxiliary medium filling the space between the blocks, are supplied below with asterisks. Parameters ε^*

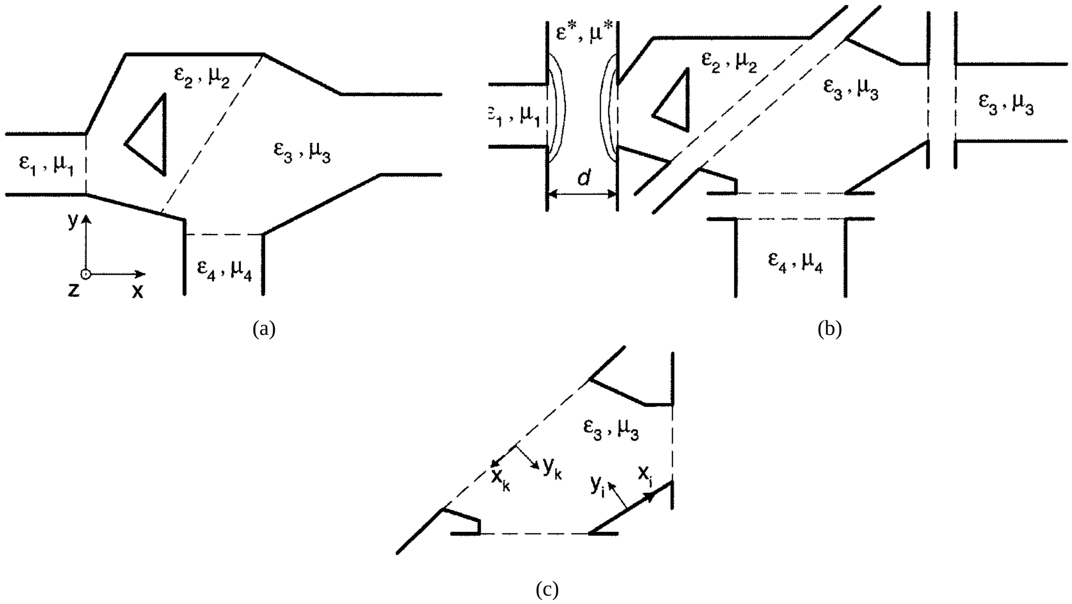

Fig. 1. Decomposition of the waveguide junction. (a) Initial unit. (b) Decomposition scheme. (c) Separate building block.

and μ* are usually considered to be equal to ε and μ of the right- or left-hand-side autonomous block.

The scattering matrix of the separate block shown in Fig. 1(c) can be determined as follows. The block is formed by an interior region, bounded by a polygon, and attached half-planes. The total field in the half-plane consists of a possible incident wave, caused by the opposite building block, and waves propagating from the flanged aperture and obeying the radiation condition. Here, we suppose that the sought-for function satisfies the homogeneous Neumann boundary condition on the flanges in both the (H) and (E) cases.

We introduce the following notations for the interior region: I_A is the set of numbers for segments related to apertures, I_D and I_N are sets for segments with Dirichlet and Neumann boundary conditions, correspondingly, and $I = I_A \cup I_D \cup I_N$. We next define local Cartesian (x_i, y_i) and elliptic (ξ_i, η_i) coordinate systems related to each other by formulas

$$x_i = f_i \cosh \xi_i \cos \eta_i \quad y_i = f_i \sinh \xi_i \sin \eta_i, \qquad i \in I \tag{4}$$

where f_i is a half-length of the ith segment. The origin of the system (x_i, y_i) is located at the center of the segment, and axis Oy_i is directed into the interior region along the normal to the perimeter. Every segment of the contour may then be taken for a degenerate ellipse $\xi_i = 0$. On its different sides, where $y_i = 0-$ or $y_i = 0+$, the variable η_i runs from $-\pi$ to 0 and from π to 0, respectively. In the coordinate systems introduced, boundary conditions take the following form:

$$U = 0 \quad y_i = 0+ \quad |x_i| < f_i, \qquad i \in I_D \tag{5}$$

$$\frac{\partial U}{\partial y_i} = 0 \quad y_i = 0+ \quad |x_i| < f_i, \qquad i \in I_N \tag{6}$$

$$\left.\frac{\partial U_i^*}{\partial \eta_i}\right|_{\eta_i=-\pi+} = \left.\frac{\partial U_i^*}{\partial \eta_i}\right|_{\eta_i=0-} = 0, \qquad i \in I_A \tag{7}$$

$$U|_{y_i=0+} = U_i^*|_{y_i=0-},$$
$$\left.\frac{\partial U}{\partial y_i}\right|_{y_i=0+} = P_i \left.\frac{\partial U_i^*}{\partial y_i}\right|_{y_i=0-} \quad |x_i| < f_i, \qquad i \in I_A. \tag{8}$$

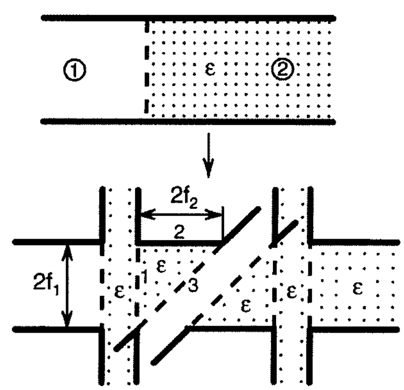

Fig. 2. Jump of permittivity and segmentation used ($f_1/f_2 = 1, \varepsilon = 2.3, \mu = 1$).

Here, U_i^* is the sought-for function within the ith half-plane and P_i is the value of the parameter P from (2) for the ith aperture (medium A is located in the interior).

Following the DPT, we consider the interior region as a common part (product) of some simple basis regions $\xi_i > 0 (i \in I)$ possessing separable geometry in the elliptic coordinates introduced. It gives possibility to represent function U in a manner similar to that in [9] and [10] as

$$U = \sum_{i \in I} U_i \tag{9}$$

$$U_i = \sum_{n=0}^{\infty} D_n^i M_n(\xi_i, q_i) ce_n(\eta_i, q_i). \tag{10}$$

Here, $ce_n(\eta_i, q_i)$ are even angular Mathieu functions, $M_n(\xi_i, q_i) = Me_n^{(2)}(\xi_i, q_i)/Me_n^{(2)}(0, q_i), Me_n^{(2)}(\xi_i, q_i)$ are relevant radial Mathieu functions (the notation are due to [11]), $q_i = (\chi f_i/2)^2$, and $\{D_n^i\}$ is a sequence of expansion coefficients to be specified. The last sequence tends to zero with increase of n as $O(1/n^{2+\chi})$ if the transverse components of the field have singularities of the type $O(r^{-\gamma})$ in

TABLE I
DEPENDENCIES OF THE S-MATRIX ELEMENTS ON THE TRUNCATION NUMBER N FOR $M_1 = M_2 = N_1 = N_2 = N_3 = N$

N	(H): $2f_1/\lambda = 0.75$				(E): $2f_1/\lambda = 0.25$			
	$\lvert S^{11}_{11}\rvert$	arg S^{11}_{11}	$\lvert S^{21}_{11}\rvert$	arg S^{21}_{11}	$\lvert S^{11}_{00}\rvert$	arg S^{11}_{00}	$\lvert S^{21}_{00}\rvert$	arg S^{21}_{00}
1	0.3062	3.1285	0.1978	-0.0086	0.2647	2.1227	0.7084	-2.1536
2	0.3665	3.0414	0.6928	-0.1722	0.2430	-0.0579	0.9735	-2.3663
4	0.3021	3.0809	0.9435	-0.0998	0.2054	0.0051	0.9786	-2.3839
6	0.2924	3.1398	0.9564	-0.1357	0.2054	0.0010	0.9787	-2.3825
8	0.2927	-3.1414	0.9562	-0.1361	0.2053	0.0003		-2.3824
10		-3.1416		-0.1360		0.0001		-2.3824
12						0.0000		-2.3822
Exact value	0.2927	-3.1416	0.9562	-0.1360	0.2053	0.0000	0.9778	-2.3822

the vicinities of the ends of the segment [9]. Here, $\chi = 1 - 2\gamma$ and γ is the greatest of two powers corresponding different end points. Since $ce_n(\eta, q) \sim \cos n\eta$, $M_n(\xi, q) \sim e^{-n\xi}$ as $n \to \infty$, (9) and (10) give efficient representation of the sought-for field in the interior.

Half-planes, attached to the apertures, also have separable geometry in elliptic coordinates. Therefore, functions U_i^*, satisfying boundary conditions (7) can be also written in the form of expansions in terms of the Mathieu functions as

$$U_i^* = \sum_{n=0}^{\infty} s_{np}^{ik} M_n(\xi_i, q_i^*) \cdot ce_n(\eta_i, q_i^*) + \delta_{ik}(-1)^p M_p(\xi_k, q_k^*) \cdot ce_p(\eta_k q_k^*), \qquad i, k \in I_A. \tag{11}$$

Here, s_{np}^{ik} are elements of the scattering matrix, subject to definition, δ_{ik} is the Kroneker delta, and k is the number of the aperture being excited. Similar to $\{D_n^i\}$, convergence rate of the sequence $\{s_{np}^{ik}\}$ depends on the behavior of the U_i^* in the vicinities of the end points of the aperture. In (11), the second term represents an incident wave propagating from the next block. The incident field expression is written in the coordinate system of the kth aperture of the block considered. It is valid solely if the distance d between that block and the next one, causing this wave, vanishes. Note that reflected waves with $n \neq p$ are orthogonal to the impinging wave in terms of inner product $(f, g) = \int_0^\pi f(\eta_k) g(\eta_k)\, d\eta_k$ for $d = 0$ only.

Inserting (9)–(11) into (5)–(8) and using orthogonal properties of the angular Mathieu functions yield the infinite linear algebraic system

$$D_m^i + \sum_{\substack{j \in I \\ j \neq i}} \sum_{n=0}^{\infty} a_{mn}^{ij} D_n^j = 0, \qquad m = \overline{0, \infty}; \quad i \in I_D \cup I_n \tag{12}$$

$$D_m^i + \sum_{j \in I} \sum_{n=0}^{\infty} a_{mn}^{ij} D_n^j + \sum_{n=0}^{\infty} b_{mn}^i s_{np}^{ik} = \delta_{ik} c_{mp}^i, \qquad m = \overline{0, \infty}; \quad i \in I_A \tag{13}$$

$$\sum_{j \in I} \sum_{n=0}^{\infty} a_{mn}^{ij} D_n^j + s_{mp}^{ik} = \delta_{ik}^* c_{mp}^i, \qquad m = \overline{0, \infty}; \quad i \in I_A \tag{14}$$

with

$$a_{mn}^{ij} = \frac{2}{\pi} \int_0^\pi \left[M_n(\xi_j, q_j) \cdot ce_n(\eta_j, q_j) \right]_{\xi_i = 0} \cdot ce_m(\eta_i, q_i)\, d\eta_i, \qquad i \in I_D \tag{15}$$

$$a_{mn}^{ij} = \frac{2}{\pi M_m'(0, q_i)} \int_0^\pi \frac{\partial}{\partial \xi_i} \left[M_n(\xi_j, q_j) \cdot ce_n(\eta_j, q_j) \right]_{\xi_i = 0} \cdot ce_m(\eta_i, q_i)\, d\eta_i, \qquad i \in I_N \tag{16}$$

$$b_{mn}^i = -\frac{2}{\pi} \int_0^\pi ce_n(\eta_i, q_i^*) ce_m(\eta_i, q_i)\, d\eta_i \tag{17}$$

$$c_{mp}^i = (-1)^{p+1} b_{mp}^i \tag{18}$$

$${}^*a_{mn}^{ii} = -\frac{M_n'(0, q_i) b_{nm}^i}{P_i M_m'(0, q_i^*)} \tag{19}$$

$${}^*a_{mn}^{ij} = \frac{2}{\pi P_i M_m'(0, q_i^*)} \int_0^\pi \frac{\partial}{\partial \xi_i} \left[M_n(\xi_j, q_j) ce_n(\eta_j, q_j) \right]_{\xi_i = 0} \cdot ce_m(\eta_i, q_i^*)\, d\eta_i, \qquad j \neq i \tag{20}$$

$${}^*c_{mp}^i = (-1)^{p+1} \delta_{mp} \tag{21}$$

Here, $M_m'(\xi, q)$ denotes the derivative of the function $M_m(\xi, q)$ with respect to ξ. The system (12)–(21) has the same properties as the one in [10] and can be solved using a truncation procedure.

The generalized scattering matrix of the open-ended waveguide consists of the amplitudes of elliptic waves of the half-space and those for the waveguide eigenmodes. It is evaluated by using an algorithm similar to the one described in [12]. Once scattering matrices of all the building blocks have been derived, one can calculate the S-matrix of the whole junction using known $[1, 3]$ reconstruction formulas.

III. SAMPLE RESULTS

Included in this section are sample results obtained from a FORTRAN computer code, which implements the theory described above. The computing periods reported below refer to an IBM PC compatible computer with a Pentium central processing unit (CPU) at 166 MHz. S_{np}^{rs} are elements of the S-matrix of the whole junction considered.

First, for the sake of verification, we examine simple waveguide discontinuity shown in Fig. 2 and formed by a jump of permittivity. Table I shows changes in S_{np}^{rs} with increasing truncation number N. N_i denotes the order of the partial sum in (10) after truncation for the functions U_i related to the middle building block. M_1 and M_2 are the numbers of the waveguide eigenmodes taken into account in ports 1 and 2 during computation. Exact values of the S_{np}^{rs} are also given. Note that

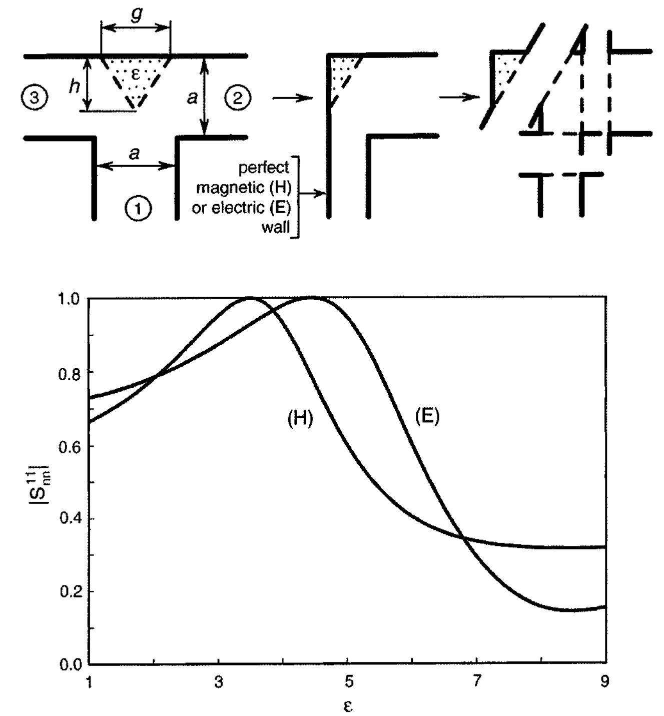

Fig. 3. $|S_{nn}^{11}|$ versus ε for a T-junction with dielectric wedge. (H): $n = 1$, $h/a = 0.2439$, $g/a = 0.7317$, $a/\lambda = 0.82$. (E): $n = 0$, $h/a = 0.5$, $g/a = 1$, $a/\lambda = 0.4$, $b = \infty$.

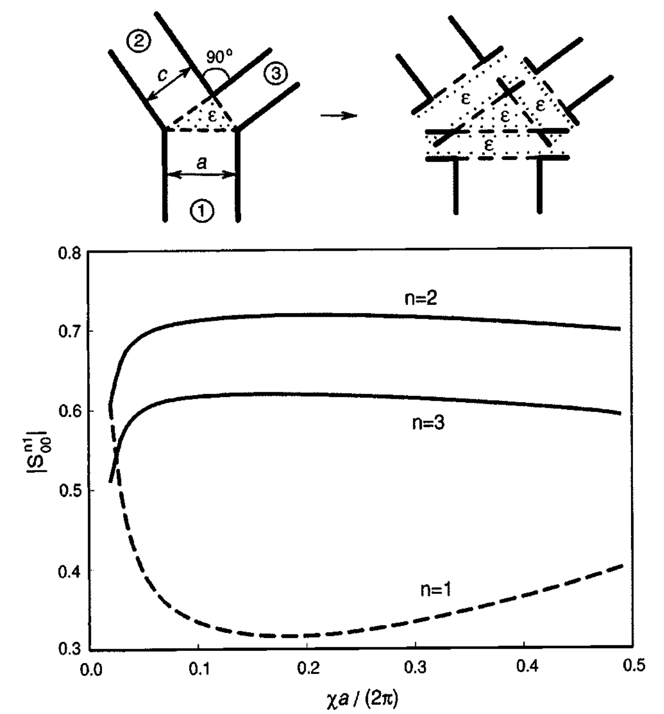

Fig. 4. $|S_{00}^{n1}|$ versus $\chi a/(2\pi)$ in the (E) case for a three-port junction with dielectric insertion ($\varepsilon = 2.3$, $\mu = 1$, $c/a = 0.8$, $b/a = 2$).

the decomposition scheme of the above object is artificially complicated to make the algorithm approximately as complex as the ones for the following examples where exact solutions are unknown. It follows from Table I that the data obtained converge rapidly to the exact values of the evaluated quantities. As seen, getting sufficiently accurate results does not lead to matrix equations of a high order and, as a consequence, does not require a large computer memory.

In Figs. 3 and 4, illustrative examples demonstrating some possibilities of the technique are given. Fig. 3 presents plots of $|S_{nn}^{11}|$ as functions of the relative permittivity of a dielectric wedge placed into the coupling cavity of the waveguide T-junction depicted. The structure is excited by the dominant mode in both the (H) and (E) cases. If $\varepsilon = 1$, results obtained coincide with the known [2] data for the respective hollow-waveguide discontinuities. The total computing periods were 6 s (H) and 8 s (E) (41 calculation points for each case).

Fig. 4 presents the dependencies of the normalized S-matrix elements versus frequency parameter $\chi a/(2\pi)$ for the three-port junction shown. The incident wave is LE_{01}. The elapsed period (26 frequency points) was 12 s.

IV. Conclusion

A new version of utilization of the generalized scattering matrix method in simulation of the two-dimensional (2-D) waveguide structures having polygonal boundaries and piecewise homogeneous fillings is presented in this paper. A special way of segmentation of such objects, providing possibility of determining S-matrices of the building blocks on the basis of the DPT, is proposed. Practical applicability of the theory has been confirmed by solving test problems. The approach offered enables efficient and accurate analysis of the wide group of geometrically complicated waveguide junctions and components with low computational cost.

Acknowledgment

The authors would like to thank the reviewers for their helpful comments and Dr. N. Yashina for her useful remarks in the preparation of this paper.

References

[1] R. Mittra and S. W. Lee, *Analytical Techniques in the Theory of Guided Waves*. New York: Macmillan, 1971.

[2] V. P. Shestopalov, A. A. Kirilenko, and A. A. Rud, *Resonance Wave Scattering, Vol. 2* (in Russian). Kiev, Russia: Naukova Dumka, 1986.

[3] V. V. Nykolsky and T. I. Nykolskaya, *Decomposition Approach to Problems in Electrodynamics* (in Russian). Moscow, Russia: Nauka, 1983.

[4] K. Ise and M. Koshiba, "Numerical analysis of H-plane waveguide junctions by combination of finite and boundary elements," *IEEE Trans. Microwave Theory Tech.*, vol. 36, pp. 1343–1351, Sept. 1988.

[5] J. Abdulnour and L. Mrildon, "Boundary elements and analysis expansions applied to H-plane waveguide junctions," *IEEE Trans. Microwave Theory Tech.*, vol. 42, pp. 1038–1045, June 1994.

[6] G. Conciauro, P. Arcioni, M. Bressan, and L. Perregrini, "Wide-band modeling of arbitrarily shaped H-plane waveguide components by the 'Boundary integral-resonant mode expansion method'," *IEEE Trans. Microwave Theory Tech.*, vol. 44, pp. 1057–1066, July 1996.

[7] F. Arndt, R. Beyer, J. M. Reiter, T. Sieverding, and T. Wolf, "Automated design of waveguide components using mode-matching/numerical EM building-blocks in optimization-oriented CAD frameworks—State-of-the-art and recent advances," *IEEE Trans. Microwave Theory Tech.*, vol. 45, pp. 747–760, May 1997.

[8] V. P. Shestopalov, A. A. Kirilenko, and S. A. Masalov, *Convolution-Type Matrix Equations in the Theory of Diffraction* (in Russian). Kiev, Russia: Naukova Dumka, 1984.

[9] V. P. Chumachenko, "Grounding of the method for solution of two-dimensional problems of electromagnetic wave diffraction on polygonal structures having perfect conductivity," *Radiotekh. Elektron.*, vol. 33, pp. 1600–1609, Aug. 1988.

[10] V. P. Chumachenko, E. Karachuha, and M. Dumanli, "An analysis of TE-scattering from a multiangular groove in a ground plane," *J. Elect. Waves Appl.*, vol. 13, pp. 381–396, Mar. 1999.

[11] N. W. McLachlan, *Theory and Application of Mathieu Functions*. New York: Dover, 1964.

[12] V. F. Burov and A. G. Chemoversky, "Dielectric-filled flange waveguide radiation," *Radiotekh. Elektron.*, vol. 28, pp. 881–887, May 1983.

Efficient Evaluation of Spatial-Domain MoM Matrix Entries in the Analysis of Planar Stratified Geometries

Noyan Kinayman and M. I. Aksun

***Abstract*—An efficient hybrid method for evaluation of spatial-domain method-of-moments (MoM) matrix entries is presented in this paper. It has already been demonstrated that the introduction of the closed-form Green's functions into the MoM formulation results in a significant computational improvement in filling up MoM matrices and, consequently, in the analysis of planar geometries. To achieve further improvement in the computational efficiency of the MoM matrix entries, a hybrid method is proposed in this paper and, through some examples, it is demonstrated that it provides significant acceleration in filling up MoM matrices while preserving the accuracy of the results.**

***Index Terms*—Closed-form spatial-domain Green's functions, method of moments, printed circuits.**

I. Introduction

The method of moments (MoM) is one of the widely used numerical techniques employed for the solution of mixed potential integral equations (MPIE's) [1]–[3] arising in the analysis of planar stratified geometries. Recently, the computational burden of the spatial-domain MoM, which is evaluations of the Sommerfeld integrals, has been alleviated by introducing an efficient algorithm to approximate these integrals in closed-form expressions, resulting in closed-form spatial-domain Green's functions [4], [5]. Consequently, the central processing unit (CPU) time required to calculate the MoM matrix entries, also known as "fill-time," has been reduced considerably. Following this development, it was also shown that the reaction integrals (MoM matrix entries) resulting from the application of the MoM in conjunction with the closed-form Green's functions can also be evaluated analytically, which further improves the computational efficiency of the spatial-domain MoM [6].

In this paper, a new hybrid method based on the use of the technique outlines in [6], in the vicinity of the source and a simpler approximation algorithm, elsewhere, is developed and presented. It is also demonstrated that this hybrid method has significantly accelerated the matrix fill-in time as compared to the original approach presented in [6]. The application of the hybrid method is provided for a realistic example, and possible difficulties together with their remedies are discussed.

II. The Hybrid Method

Evaluation of MoM matrix entries is the one that requires most of the CPU time of the technique for moderate-size geometries (spanning a few wavelengths). To give an idea, CPU times for the evaluations of the Green's functions, matrix entries, and the solution of the MoM matrix equation are given in Table I for some typical printed geometries. Note that the geometries referred to in Table I have been analyzed with uniform segmentation, which gives rise to block symmetric MoM impedance matrices. Detailed study of hybrid method for the interdigital capacitor mentioned in Table I will be provided in the following sections. Due to space limitations, results for the patch antenna and the bandpass filter could not be provided.

In order to introduce the hybrid method, let us first write down the spatial-domain MoM matrix entry of a planarly stratified geometry obtained through the MPIE formulation [1], [2]

$$Z_{mn} = \langle T_{xm}, G_{xx}^A * J_{xn} \rangle + \frac{1}{w^2} \left\langle T_{xm}, \frac{\partial}{\partial x}\left[G_x^q * \frac{\partial J_{xn}}{\partial x}\right]\right\rangle \tag{1}$$

where T_{xm} are the testing functions, J_{xn} are the basis functions, and $\langle\, , \rangle$ is the inner product. The spatial-domain Green's functions employed in (1) are obtained in closed forms with the use of the two-level approach described in [7], which have the generic form of

$$G^{A,q} \cong \sum_{n=1}^{N} a_n \frac{e^{-jk_i r_n}}{r_n} \tag{2}$$

where $r_n = \sqrt{\rho^2 - b_n^2}$, $\rho = \sqrt{x^2+y^2}$, k_i is the wavenumber in source layer, and b_n is the complex constant. It has been demonstrated in [6] that the MoM matrix entries given in (1) can be calculated analytically without any numerical integration for piecewise-continuous basis and testing functions, provided the closed-form Green's functions are used for the formulation. In that approach, each of the exponentials in (2) is replaced by its Taylor series approximation as follows:

$$G^{A,q} \cong \sum_{n=1}^{N} a_n \sum_{m=0}^{M} c_{mn} \frac{(r_n - r_c)^m}{r_n} \tag{3}$$

where c_{mn} are the Taylor series coefficients and r_c is the center of expansion for the exponential term $e^{-jk_i r_n}$. Alternatively, one could replace the entire Green's function in (2) with a suitable approximation that would enable the reaction integrals to be evaluated analytically. For instance, one may use the polynomial approximation for the Green's function as

$$G^{A,q} \cong \sum_{l=-1}^{L} \gamma_l \cdot \rho^l \tag{4}$$

where γ_l are complex coefficients obtained from a least-squares (LS) fitting scheme. It is obvious that the analytical integration of the reaction integrals is considerably simpler for the Green's function expressed in (4) than for those expressed in (3). This is because the analytical evaluation of the inner-product integrals using the former representation requires extensive complex arithmetic operations, as well as multiple evaluations of complex logarithms and trigonometric functions. However, the caveat in the polynomial-fitting approach is that the approximating the Green's function over the entire range is very difficult, if not impossible, with a relatively small L, because of the singular behavior of the Green's functions as $\rho \to 0$. One approach to resolving this dilemma is to utilize both of the above representations, but in complementary regions, thereby taking the advantage of the salient features of both. This can be done by using (3) to represent the Green's function for small ρ, where it exhibits a singular behavior, and then by switching over to (4) as ρ becomes larger.

To summarize, a direct application of the rigorous method places an unnecessary computational burden when ρ, the distance between the source and testing points, is greater than a predetermined value $\rho_{ls} = 10^s/k_0$, where s is a constant. To circumvent this problem, one can use a hybrid approach as given in (5), which uses a judicious combination

Manuscript received November 4, 1997.

N. Kinayman is with the Corporate Research and Development Department, M/A-COM, Lowell, MA 08153 USA.

M. I. Aksun is with the Department of Electrical and Electronics Engineering, Bilkent University, Ankara 06533, Turkey.

Publisher Item Identifier S 0018-9480(00)00864-4.

TABLE I
CPU TIMES IN SECONDS REQUIRED FOR THE ANALYSIS OF SOME TYPICAL GEOMETRIES AT SINGLE FREQUENCY ON A SUN SPARC ULTRA-2 WORKSTATION. HYBRID METHOD INCLUDES THE ADAPTIVE SELECTION OF ρ_{ls}, AS EXPLAINED IN SECTION II

Geometry	# of unknowns	Analysis frequency (MHz)	Green's function computation time (sec.)	Matrix fill-time (sec.)		Solution time (sec.)
				Hybrid	Rigorous	
Patch antenna [8]	537	2300	2.3	7	63	30
Band-pass filter [9]	1638	2575	2.3	23	570	1100
Interdigital MIC capacitor (Fig. 1)	576	5500	2.3	9	187	39

of the two methods, to increase the computational speed with which the MoM matrix entries are generated as follows:

$$Z_{mn}^{q,A} = \begin{cases} \int\int f(u)g(v) \sum_{n=1}^{N} a_n \frac{e^{-jk_i\sqrt{u^2+v^2-b_n^2}}}{\sqrt{u^2+v^2-b_n^2}}\, du\, dv, & \rho < \rho_{ls} \quad (5a) \\ \int\int f(u)g(v) \sum_{l=-1}^{L} \gamma_l \rho^l\, du\, dv, & \rho \geq \rho_{ls}. \quad (5b) \end{cases}$$

For rooftop basis and testing functions, $f(u)$ and $g(v)$ are given as

$$f(u) = \alpha_0 + \alpha_1 u + \alpha_2 u^2 + \alpha_3 u^3 \quad (6)$$

$$g(v) = \beta_0 + \beta_1 v \quad (7)$$

where α and β are constants obtained from the correlation operation of the basis and testing functions [6].

At this point, it is worthwhile to describe the strategy for employing the hybrid technique. To use a small L in (4) and simplify the algorithm, the polynomial-fitting algorithm is performed over a small range of ρ, which is requires the LS fitting with N_{ls} sampling points to be repeated for each of the inner-product operations. Consequently, to accelerate the fitting process, the closed-form Green's function is sampled between ρ_{ls} and $\rho_{\max}$, and the sampled values are stored in a look-up table before starting to fill up the MoM matrix. These tabulated values can then be subsequently interpolated to perform the LS fitting relatively fast for each inner product operation. Here, one can use linear or quadratic interpolation scheme to find required values for the LS approximation process from the previously sampled values of the Green's function whose effects will also be demonstrated.

For a given geometry, either user can specify the value of ρ_{ls} through s or it can be determined adaptively by using the rms fitting error in the LS approximation scheme. The adaptive approach, which is the one used throughout this paper, starts with an error criterion defined as in following form:

$$\sqrt{\frac{1}{N_e}\sum_{i=0}^{N_e}\left[G_{\text{method }\#1}^{A,q} - G_{\text{method }\#2}^{A,q}\right]^2} \leq E \quad (8)$$

where $G_{\text{method }\#1}^{A,q}$ corresponds to the Green's function approximations obtained from (3), $G_{\text{method }\#2}^{A,q}$ corresponds to the Green's function approximations obtained from (4), E is the acceptable rms fitting error, and N_e is the number of samples used in error checking ($N_e > N_{ls}$). Then, since the LS approximation in (4) is implemented over a range of $\rho(\rho_a \leq \rho \leq \rho_b)$, the lower and upper limits ρ_a and ρ_b, respectively, are determined adaptively starting with the initial values of minimum cell width and maximum possible ρ value for the inner product evaluation, respectively. If the condition specified by (8) is satisfied, ρ_{ls} is set to ρ_a and the iteration is terminated, otherwise ρ_a is increased by a small increment $\Delta\rho$, and the iteration continues until (8) is satisfied. This approach makes the hybrid method a very suitable tool for designing an efficient MoM-based electromagnetic simulator. In the examples given in Table I, the constant E was selected as 10^{-5}.

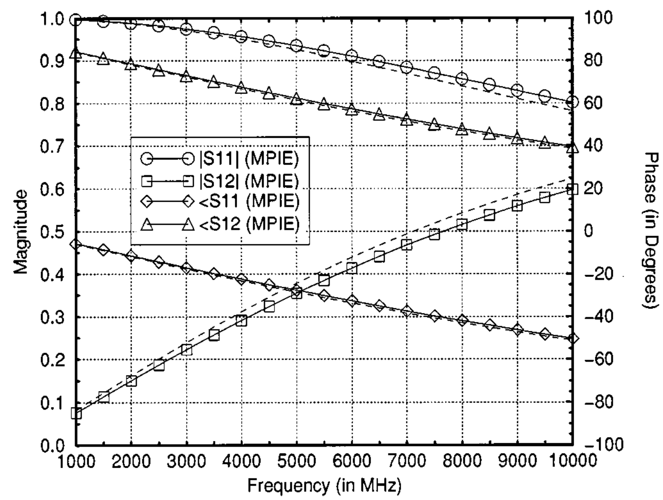

Fig. 1. S_{11} and S_{12} of the interdigital capacitor given in Fig. 2. The dashed lines represent the results from ***em*** by Sonnet Software, Inc, Liverpool, NY.

III. NUMERICAL EXAMPLES

To study the effectiveness and accuracy of the hybrid method proposed in this paper, CPU times for different parameter setting and scattering parameters (S-parameters) of an example printed structure are obtained using the rigorous and hybrid methods. The example selected here is an interdigital microwave integrated circuit (MIC) capacitor whose S-parameters and geometry are shown in Figs. 1 and 2, respectively. Number of basis functions for the interdigital capacitor is chosen to be 576. For the sake of fairness, an error term is defined as

$$\text{error} = \sqrt{\sum_{i=1}^{N_p}\left|S_{1i}^{\text{rigorous}} - S_{1i}^{\text{hybrid}}\right|^2} \quad (9)$$

where N_p is the number of ports in the structure. The matrix fill time for this geometry could be reduced by changing the auxiliary parameter s, as shown in Fig. 2 ($L = 4,\ N_{ls} = 9$). Note that the matrix fill time for each s value given in the figure is the accumulative fill time over frequency in the simulation band, whereas the times given in Table I are at single frequency. To find the average fill time at a single frequency, the

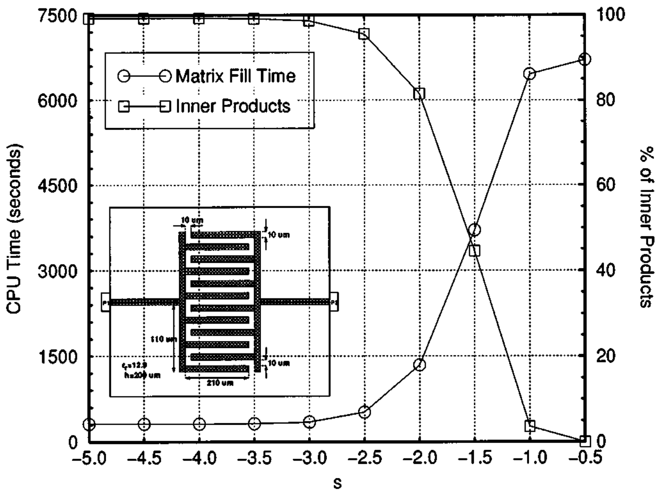

Fig. 2. Total matrix and percentage of inner-products that fall in the LS approximation region for the interdigital capacitor (1000 MHz $\leq f \leq 10\,000$ MHz, $\Delta f = 250$ MHz).

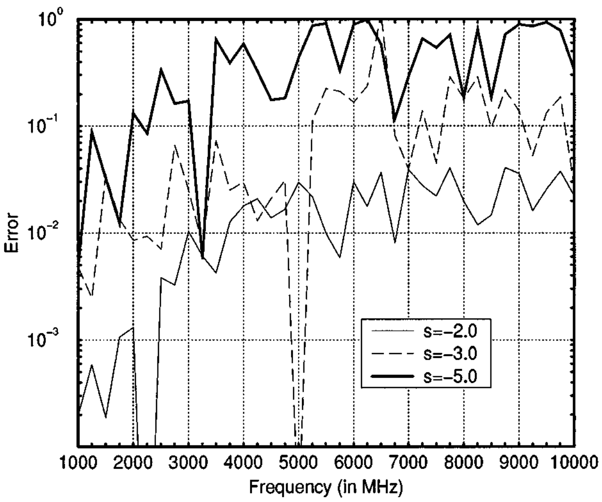

Fig. 3. Error in S_{11} and S_{12} of the interdigital capacitor for different values of s [error is defined in (9)].

time values read from Fig. 2 should be divided by the number of simulation points, which in this case is 37. From the figure, it is observed that the matrix fill time is saturated around $s = -3.0$, providing a considerable amount of reduction in the matrix fill time. However, the error in S-parameters is relatively high at some frequency points, and the situation is even worse at $s = -5.0$, as shown in Fig. 3. This could be attributed to a poor approximation of the Green's functions by the polynomials given in (4). It is also observed that the error in S-parameters increases even though the percentage of the inner products evaluated through the LS fitting scheme does not increase. This is due to fact that, although the value of ρ_{ls} below some point cannot change the matrix fill time (unless it becomes zero), the algorithm keeps sampling the Green's functions starting from lower and lower ρ values as ρ_{ls} is decreasing. However, such choices of ρ_{ls} only occur in cases of manually varying the value of s; in practice, there is a minimum limit (usually the minimum cell width) on the value of ρ_{ls} and it is determined by the adaptive algorithm that was previously described.

As a next step, the number of sampling points, i.e., N_{ls}, is increased from 9 to 12, and the error in S-parameters is calculated again for $s = -5.0$, giving the results in Fig. 4. While there is a noticeable improvement in the average error, the error is still not acceptable at higher frequency points. Thus far, we have only employed linear interpolation with nine interpolation points, for which the results given in Fig. 3 have higher error for $s = -5.0$. Although increasing the interpolation points from 9 to 12 in the linear LS approximation has improved the results to a degree, they are still not acceptable (Fig. 4). However, switching to quadratic interpolation from linear interpolation gives a significant improvement even for the smaller values of s, as shown in Fig. 4.

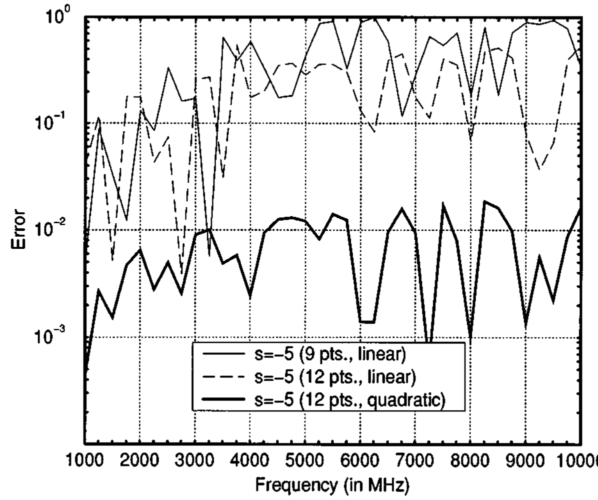

Fig. 4. Error in S_{11} and S_{12} of the interdigital capacitor for different values of s [error is defined in (9)].

IV. Conclusions

In this paper, it has been demonstrated that the hybrid method significantly improves the efficiency of the evaluation of spatial-domain MoM matrix entries, on the order of tenfold to twentyfold reduction in matrix fill time. Therefore, even for moderate-size geometries, the solution time of the matrix equations becomes the dominating factor on the overall performance of the spatial-domain MoM. Consequently, the spatial-domain MoM in conjunction with the closed-form Green's functions has become a powerful computer-aided design (CAD) tool for the analysis of planar structures, provided that the hybrid method presented in this paper is employed in the evaluation of the matrix entries.

References

[1] J. R. Mosig and F. E. Gardiol, "General integral equation formulation for microstrip antennas and scatterers," *Proc. Inst. Elect. Eng.*, pt. H, vol. 132, pp. 424–432, Dec. 1985.
[2] J. R. Mosig, "Arbitrarily shaped microstrip structures and their analysis with a mixed potential integral equation," *IEEE Trans. Microwave Theory Tech.*, vol. 36, pp. 314–323, Feb. 1988.
[3] W. C. Chew, *Waves and Fields in Inhomogeneous Media*. New York: Van Nostrand, 1990.
[4] Y. L. Chow, J. J. Yang, D. G. Fang, and G. E. Howard, "A closed-form spatial Green's function for the thick microstrip substrate," *IEEE Trans. Microwave Theory Tech.*, vol. 39, pp. 588–592, Mar. 1991.
[5] M. I. Aksun and R. Mittra, "Derivation of closed-form Green's functions for a general microstrip geometry," *IEEE Trans. Microwave Theory Tech.*, vol. 40, pp. 2055–2062, Nov. 1992.
[6] L. Alatan, M. I. Aksun, K. Mahadevan, and T. Birand, "Analytical evaluation of MoM matrix elements," *IEEE Trans. Microwave Theory Tech.*, vol. 44, pp. 519–525, Apr. 1996.
[7] M. I. Aksun, "A robust approach for the derivation of closed-form Green's functions," *IEEE Trans. Microwave Theory Tech.*, vol. 44, pp. 651–658, May 1996.
[8] D. M. Pozar, "Input impedance and mutual coupling of rectangular microstrip antennas," *IEEE Trans. Antennas Propogat.*, vol. AP-30, pp. 1191–1196, Nov. 1982.

[9] J.-S. Hong and M. J. Lancaster, "Couplings of microstrip square open-loop resonators for cross-coupled planar microwave filter," *IEEE Trans. Microwave Theory Tech.*, vol. 44, pp. 2099–2109, Dec. 1996.

CAD Models for Asymmetrical, Elliptical, Cylindrical, and Elliptical Cone Coplanar Strip Lines

Zhengwei Du, Ke Gong, Jeffrey S. Fu, Zhenghe Feng, and Baoxin Gao

***Abstract*—By the conformal mapping method, we give analytical closed form expressions for the quasi-TEM parameters for asymmetrical coplanar strip lines (ACPS's) with finite boundary substrate. Then, based on the analysis of ACPS's, elliptical coplanar strip lines (ECPS's) and cylindrical coplanar strip lines (CCPS's), and elliptical cone coplanar strip lines (ECCPS's) are studied. Computer-aided-design oriented analytical closed-form expressions for the quasi-TEM parameters for ACPS's, ECPS's, CCPS's, and ECCPS's are obtained. All of the expressions are simple and accurate for microwave circuits' designs and are useful for transmission-line theory and antenna theory. The reasonableness of the method and results are verified and various design curves are given.**

***Index Terms*—Asymmetrical coplanar strip lines, CAD modes, conformal mapping, cylindrical coplanar strip lines, elliptical cone coplanar strip lines, elliptical coplanar strip lines.**

I. Introduction

Coplanar transmission lines are used extensively in monolithic microwave integrated circuits (MMIC's) and integrated optical applications [1], [2]. An asymmetrical coplanar transmission line consists of a narrow metal strip and a conductive plane grounded, which are placed on one side of the dielectric substrate and mutually separated by a narrow slot. The advantage is the possibility of combination with other types of transmission lines such as a slot line, coplanar waveguide, and microstrip when used in filters, impedance matching networks, and directional couplers. In the earlier years, coplanar strip lines (CPS's) were analyzed by assuming that the substrate is infinite [3], [4]. In recent years, people obtained the expressions for the quasi-TEM parameters for CPS's on a substrate [5], [6] and multilayer substrates [7]–[10] of finite thickness. The problem of a CPS with a substrate of finite thickness and finite width has not been solved up to now.

Elliptical coplanar strip lines (ECPS's), cylindrical coplanar strip lines (CCPS's), and elliptical cone coplanar strip lines (ECCPS's) can be used as adapters and slot lines as well as antennas. Although elliptical [11] and elliptical cone [12], [13] striplines and microstrip lines have been analyzed, the analyzes of ECPS's and ECCPS's have not been reported to our knowledge. In [14] and [15] closed form expressions for quasi-TEM parameters for CCPS's were given. Both [14] and [15] treated the width of the substrate as infinite when the CCPS was mapped into the ACPS, while the width should be 2π. In addition, there is an error in [15] as pointed out in this paper.

The objective of this paper is to solve the problems mentioned above. Assuming that the ACPS with a finite-boundary dielectric substrate of finite thickness and width, ECPS, CCPS, and ECCPS are operating in the quasi-TEM mode, the conformal mapping method is used for the analysis. The assumption is valid when the length of a line is much longer than the wavelength of the guided wave and the operating frequency of the guided wave is not high. This method can give fast and accurate results in the microwave frequency range since the quasi-TEM parameters for coplanar lines are only slightly sensitive to changes in the frequency [15]. As the substratum, we study the quasi-TEM parameters for the ACPS with finite boundary substrates at first. In Sections III and IV, ECPS's, CCPS's, and ECCPS's are analyzed. In Section V, the reasonableness of the method and results are verified, and numerical results for the characteristic impedance for the ACPS with finite boundary substrate, ECPS, CCPS, and ECCPS are given.

Manuscript received May 21, 1998.

Z. Du, K. Gong, Z. Feng, and B. Gao are with the State Key Laboratory on Microwave and Digital Communications, Department of Electronic Engineering, Tsinghua University, Beijing 100084, China.

J. S. Fu is with the School of Electrical and Electronic Engineering, Nanyang Technological University, Singapore 639798, Singapore.

Publisher Item Identifier S 0018-9480(00)00863-2.

II. ACPS with Finite Boundary Substrate

The analyzed ACPS on a finite-boundary substrate is shown in Fig. 1(a). The widths of the infinitely long strips are w_1 and w_2 and the gap between them is $2s$. The two strips are mounted on a substrate having a thickness of h, a width of $2w$, and a relative dielectric constant of ε_r. In this case, the ACPS capacitance C is $C = C_0 + C_1$, where C_0 is the ACPS capacitance in free space when the dielectric is replaced by air, and C_1 is the ACPS capacitance obtained when assuming that the electric field is concentrated in a dielectric of thickness h, width $2w$, and relative dielectric constant of $\varepsilon_r - 1$. This assumption has shown an excellent accuracy in the cases of the CPS and ACPS with a finite thickness and infinite width substrate [5]–[8].

The free-space capacitance C_0 is given by [9]

$$C_0 = \varepsilon_0 \frac{K(k_0')}{K(k_0)} \tag{1}$$

where k_0 is shown in (2) at the bottom of the following page. In order to obtain the capacitance C_1, the dielectric region in Fig. 1(a) is mapped into the lower half region, as shown in Fig. 1(b), by the Jacobian elliptic function transformation $t = sn((K(k)/w)z, k)$, where $K(k)$ is the complete elliptic integral of the first kind of modulus k, $K(k)/K(k') = w/h$, and $k' = \sqrt{1-k^2}$. For simplified calculation, the excellent approximate expressions of k are given by [16]

$$k = \left[\frac{\exp(\pi w/h) - 2}{\exp(\pi w/h) + 2}\right]^2, \qquad \text{for } 1 \le \frac{w}{h} < \infty \tag{3a}$$

$$k = \sqrt{1 - \left[\frac{\exp(\pi h/w) - 2}{\exp(\pi h/w) + 2}\right]^4}, \qquad \text{for } 0 < \frac{w}{h} < 1. \tag{3b}$$

The widths s, w_1, and w_2 are mapped s_t, w_{1t}, and w_{2t}, which can be expressed as follows:

$$s_t = t_1 = sn\left(\frac{K(k)}{w}s,\, k\right) \tag{4a}$$

$$w_{1t} = t_2 - t_1 = sn\left(\frac{K(k)}{w}(s+w_1),\, k\right) - sn\left(\frac{K(k)}{w}s,\, k\right) \tag{4b}$$

$$w_{2t} = t_3 - t_1 = sn\left(\frac{K(k)}{w}(s+w_2),\, k\right) - sn\left(\frac{K(k)}{w}s,\, k\right). \tag{4c}$$

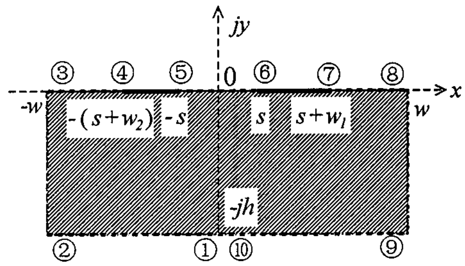

(a)

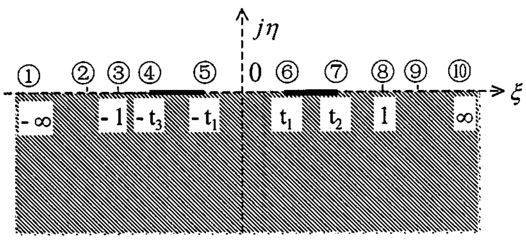

(b)

Fig. 1. Geometry of ACPS and its conformal mapping. (a) Original ACPS on z-plane. (b) t-plane.

Thus, the capacitance C_1 is given by

$$C_1 = \frac{1}{2}\varepsilon_0(\varepsilon_r - 1)\frac{K(k_1')}{K(k_1)} \tag{5}$$

where k_1 and k_1' are shown in (6), at the bottom of this page.

Therefore, the capacitance per unit length and the characteristic impedance for the ACPS can be expressed as

$$C = C_0 + C_1 = \varepsilon_0 \varepsilon_{\text{eff}} \frac{K(k_0')}{K(k_0)}$$
$$Z_0 = \frac{120\pi}{\sqrt{\varepsilon_{\text{eff}}}} \frac{K(k_0)}{K(k_0')}. \tag{7}$$

The effective dielectric constant ε_{eff} and the wavelength λ_g of the guided wave are given by

$$\varepsilon_{\text{eff}} = 1 + \frac{\varepsilon_r - 1}{2} \frac{K(k_0)}{K(k_0')} \frac{K(k_1')}{K(k_1)}$$
$$\lambda_g = \frac{\lambda_0}{\sqrt{\varepsilon_{\text{eff}}}} \tag{8}$$

where λ_0 is the wavelength in free space.

III. ECPS AND CCPS

For the cross section of an ECPS on the z_1-plane, shown in Fig. 2(a), there are two confocal ellipses. Their semimajor axes and semiminor

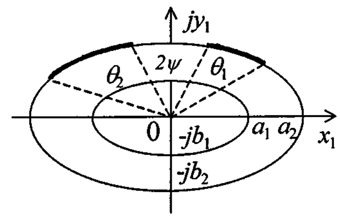

(a)

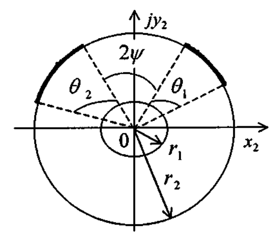

(b)

Fig. 2. ECPS. (a) z_1-plane. (b) z_2-plane.

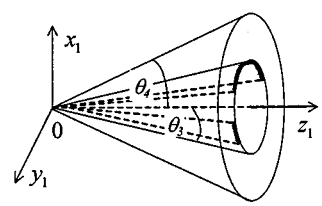

(a)

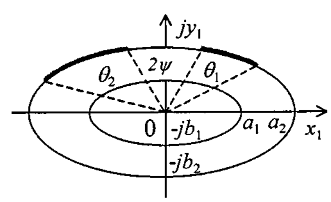

(b)

Fig. 3. ECCPS. (a) Geometry. (b) Cross section.

axes are a_1, a_2, b_1, and b_2, respectively. The angles subtended by the arc strip lines and the gap between the two strips at center are θ_1, θ_2, and 2ψ, respectively. The relative dielectric constant of the substrate is ε_r. The dimensional relationship between the two ellipses is

$$c = \sqrt{a_1^2 - b_1^2} = \sqrt{a_2^2 - b_2^2}. \tag{9}$$

$$k_0 = \frac{(w_1 + w_2 + 2s)s}{w_1 w_2 + (w_1 + w_2 + 2s)s + \sqrt{w_1^2 w_2^2 + 2w_1 w_2 s(w_1 + w_2 + 2s)}}. \tag{2}$$

$$k_1 = \frac{(w_{1t} + w_{2t} + 2s_t)s_t}{w_{1t} w_{2t} + (w_{1t} + w_{2t} + 2s_t)s_t + \sqrt{w_{1t}^2 w_{2t}^2 + 2w_{1t} w_{2t} s_t(w_{1t} + w_{2t} + 2s_t)}}$$
$$k_1' = \sqrt{1 - k_1^2} \tag{6}$$

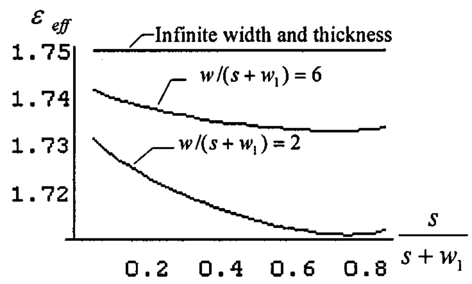

(a)

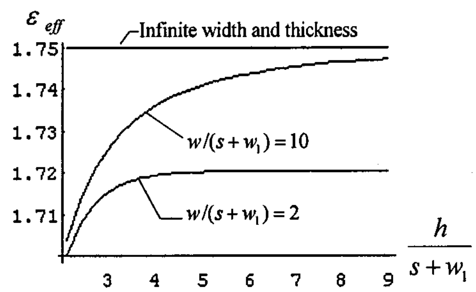

(b)

Fig. 4. The effective dielectric constant for ACPS changes ($\varepsilon_r = 2.5, w_1 = w_2$). (a) $h/(s+w_1) = 4$. (b) $s/(s+w_1) = 0.3$.

Using the transformation $z_2 = (z_1 - \sqrt{z_1^2 - c^2})/c$ [11], the structure in Fig. 2(a) is mapped into the CCPS on the z_2-plane, as shown in Fig. 2(b). Their radii are given by

$$r_1 = \sqrt{\frac{a_1 + b_1}{a_1 - b_1}} \quad r_2 = \sqrt{\frac{a_2 + b_2}{a_2 - b_2}}. \tag{10}$$

Applying the following principle logarithm $z = j \ln(z_2/r_2) + (\pi/2)$, the structure is mapped into the ACPS on the z-plane shown in Fig. 1(a). Considering (9), the structure parameters w_1, w_2, s, h, and w for the ECPS are given as follows:

$$w_1 = \theta_1 \quad w_2 = \theta_2 \quad s = \psi \tag{11a}$$

$$h = \ln \frac{r_2}{r_1} = \ln \frac{a_2 + b_2}{a_1 + b_1} \quad w = \pi \tag{11b}$$

when $a_1 = b_1 = a, a_2 = b_2 = b$, i.e., $c = 0$, h becomes $h = \ln(b/a)$, then (11) gives the structure parameters for the CCPS.

Inserting (11) into (7) and (8), we can obtain the quasi-TEM parameters for the ECPS and CCPS. By the way, the expressions of k_d and Q in [15], i.e., [15, eqs. (11) and (12)], are wrong; they should be expressed as (12), shown at the bottom of this page.

IV. ECCPS

Two infinitely long triangular arc strip lines with an elliptic cross section are mounted on an elliptic conical substrate, as shown in Fig. 3(a). The whole structure has two strip lines, the corresponding flare angles θ_1 and θ_2, two extreme flare angles θ_3 and θ_4, shaped by the inner and exterior elliptical cone, the gap between the strips 2ψ, and a relative dielectric constant of ε_r. The cross section is shown in Fig. 3(b).

The scalar Helmholtz equation for spherical-TEM waves in a spherical–conical coordinate system is given by [12] and [13]

$$\sqrt{1 - k_2^2 \cos^2 \theta} \frac{\partial}{\partial \theta} \left(\sqrt{1 - k_2^2 \cos^2 \theta} \frac{\partial U}{\partial \theta} \right) + \sqrt{1 - k_2'^2 \cos^2 \varphi} \frac{\partial}{\partial \varphi} \left(\sqrt{1 - k_2'^2 \cos^2 \varphi} \frac{\partial U}{\partial \varphi} \right) = 0 \tag{13}$$

where

$$U = \frac{e^{-j\alpha_0 r}}{r} u(\theta, \varphi) \quad \alpha_0 = \omega \sqrt{\mu \varepsilon_0 \varepsilon_r}. \tag{14}$$

If δ_1 and δ_2 are the flare angles of the focus lines of the inner and outer elliptic cones, respectively, and they satisfy $\cos\theta_3 \tan\delta_1 = \cos\theta_4 \tan\delta_2$, we then have [12]

$$\begin{aligned} k_2 &= (1 + \tan^2 \delta_1 \cos^2 \theta_3)^{-(1/2)} \\ &= (1 + \tan^2 \delta_2 \cos^2 \theta_4)^{-(1/2)} \\ k_2' &= \sqrt{1 - k_2^2}. \end{aligned} \tag{15}$$

Taking the two transformations $\alpha = F(\theta, k_2) - K(k_2)$, $\beta = F(\varphi, k_2') - K(k_2')$, where $F(\theta, k_2)$ is the incomplete elliptic integral of the first kind of modulus k_2, (13) becomes

$$\frac{\partial^2 u}{\partial \alpha^2} + \frac{\partial^2 u}{\partial \beta^2} = 0. \tag{16}$$

The structure in Fig. 3 is mapped into the ACPS on the z-plane, as shown in Fig. 1(a). The structure parameters w_1, w_2, s, h, and w are given by

$$\begin{aligned} w_1 &= F(\psi + \theta_1, k_2') - F(\psi, k_2') \\ w_2 &= F(\psi + \theta_2, k_2') - F(\psi, k_2') \end{aligned} \tag{17a}$$

$$\begin{aligned} s &= F(\psi, k_2') \\ h &= F(\theta_4, k_2) - F(\theta_3, k_2) \\ w &= 2K(k_2'). \end{aligned} \tag{17b}$$

Using (7), (8), and (17), the quasi-TEM parameters for the ECCPS are obtained.

V. Numerical Results

To illustrate that the method is reasonable, we first make a comparison between the ACPS with infinite substrates [8] and finite substrates.

$$\begin{aligned} k_d &= \sqrt{\frac{\left[\sinh(Qs) - \sinh(Q(s+2w_1))\right]\left[\sinh(Qs) - \sinh(Q(s+2w_2))\right]}{\left[\sinh(Qs) + \sinh(Q(s+2w_1))\right]\left[\sinh(Qs) + \sinh(Q(s+2w_2))\right]}} \\ Q &= \frac{\pi}{4h}. \end{aligned} \tag{12}$$

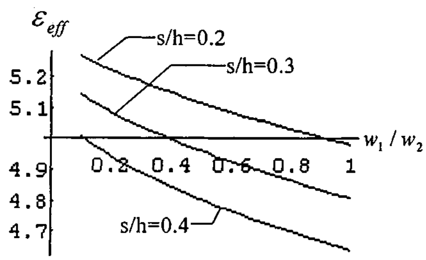

(a)

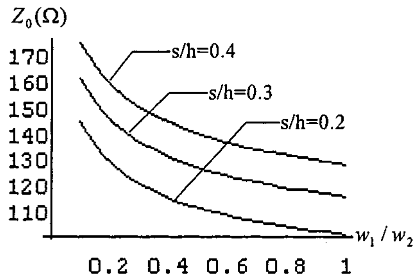

(b)

Fig. 5. The calculated results for $\varepsilon_{\rm eff}$ and Z_0 for ACPS ($\varepsilon_r = 10, w/h = 2, w_2/h = 0.5$). (a) Effective dielectric constant. (b) Characteristic impedance.

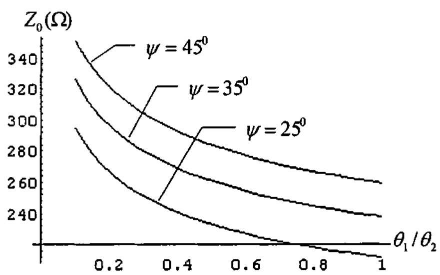

Fig. 6. Z_0 for ECPS and CCPS changes with θ_1/θ_2 ($\varepsilon_r = 2.5, \theta_2 = 40°, h = \ln 2$).

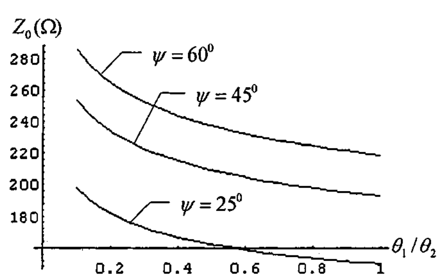

Fig. 7. Z_0 for ECCPS changes with θ_1/θ_2 ($\varepsilon_r = 10, \delta_1 = 25°, \theta_2 = 60°, \theta_3 = 20°, \theta_4 = 30°$).

Fig. 4(a) and (b) give the effective dielectric constant for the ACPS changing with $s/(s+w_1)$ and $h/(s+w_1)$, respectively. From the curves, we can find that the effective dielectric constant for the ACPS increase with the substrate width w and the thickness h. $\varepsilon_{\rm eff}$ of the ACPS with a finite substrate approaches to the value of $\varepsilon_{\rm eff}$ of the ACPS with an infinite substrate when w and h are large enough. It satisfies the fact and verifies that the method used in this paper is reasonable. Since ECPS's, CCPS's, and ECCPS's analyzed in this paper are rigorously mapped into the ACPS with finite boundary substrates whose result is the substratum of their analyses, their analyses are also reasonable.

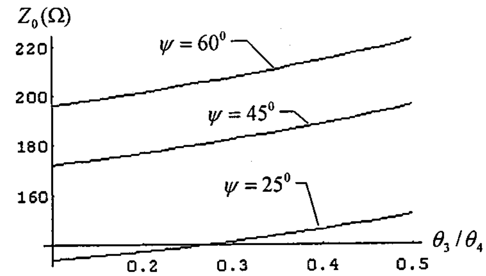

Fig. 8. Z_0 for ECCPS changes with θ_3/θ_4 ($\varepsilon_r = 10, \delta_1 = 25°, \theta_2 = 60°, \theta_3 = 20°, \theta_4 = 30°$).

As examples, we give the numerical results for the characteristic impedance Z_0 for the ACPS with a finite-boundary substrate, ECPS, CCPS, and ECCPS. Fig. 5(a) and (b) show $\varepsilon_{\rm eff}$ and Z_0 for the ACPS ($\varepsilon_r = 10, w/h = 2, w_2/h = 0.5$) as a function of the asymmetry ratio w_1/w_2 for several values of s/h. Figs. 6–8 give the changes of Z_0 for the ECPS, CCPS, and ECCPS via the structure parameters.

VI. Conclusions

The ACPS with a finite-boundary substrate is studied as the substratum of this paper. The ECPS, CCPS, and ECCPS are rigorously transformed into the ACPS with a finite boundary substrate using the conformal mapping method. The computer-aided-design (CAD) oriented analytical closed-form expressions for quasi-TEM parameters for the ACPS, ECPS, CCPS, and ECCPS are obtained. The formulations are both accurate and simple for microwave circuit and antenna designs. Various numerical results are given to show the reasonableness of the method and results, and the dependence of the characteristic impedance on the structure parameters.

Acknowledgment

The authors would like to thank the anonymous reviewers and Dr. W. J. R. Hoefer for their critical comments and helpful suggestions.

References

[1] I. Kneppo and J. Gotzman, “Basic parameters of nonsymmetrical coplanar lines,” *IEEE Trans. Microwave Theory Tech.*, vol. MTT-25, p. 718, Aug. 1977.

[2] S. S. Gevorgian, “Asymmetric coplanar-strip transmission lines for MMIC and integrated optic applications,” *Electron. Lett.*, vol. 26, no. 22, pp. 1916–1917, 1990.

[3] S. S. Bedair, “Characteristics of some asymmetrical coupled transmission lines,” *IEEE Trans. Microwave Theory Tech.*, vol. MTT-32, pp. 108–110, Jan. 1984.

[4] C. P. Wen, “Coplanar waveguide: A surface strip transmission lines suitable for nonreciprocal gyromagnetic device,” *IEEE Trans. Microwave Theory Tech.*, vol. MTT-17, pp. 1087–1090, June 1969.

[5] C. Veyres and V. F. Hanna, “Extension of the application of conformal mapping techniques to coplanar lines with finite dimensions,” *Int. J. Electron.*, vol. 48, no. 1, pp. 47–56, Jan. 1980.

[6] V. F. Hanna, “Finite boundary corrections to coplanar stripline analysis,” *Electron. Lett.*, vol. 16, no. 15, pp. 604–606, 1980.

[7] S. S. Gevorgian, “Basic characteristics of two layered substrate coplanar waveguides,” *Electron. Lett.*, vol. 30, no. 15, pp. 1236–1237, 1994.

[8] E. Chen and S. Y. Chou, “Characteristics of coplanar transmission lines on multilayers substrates: Modeling and experiments,” *IEEE Trans. Microwave Theory Tech.*, vol. 45, pp. 939–945, June 1997.

[9] Z. Du and C. Ruan, “Basic parameters of asymmetrical coplanar striplines with finite substrate thickness” (in Chinese), *J. Electron.*, vol. 20, no. 6, pp. 828–834, Nov. 1998.

[10] Z. Du, J. S. Fu, and K. Gong, “Basic parameters of asymmetrical coplanar striplines with multilayer substrates and overlays,” *Int. J. Infrared Millim. Waves*, vol. 20, no. 2, pp. 351–356, Feb. 1999.

[11] L.-R. Zeng and Y. Wang, "Accurate solutions of elliptical and cylindrical striplines and microstrip lines," *IEEE Trans. Microwave Theory Tech.*, vol. MTT-34, pp. 259–265, Feb. 1986.
[12] W. Lin, *Lin Weigan's Selected Works in Microwave Field Theory and Application Study* (in Chinese). Beijing, China: Publication House Electron. Ind., 1989, pp. 180–183.
[13] N. Yuan, C. Ruan, and W. Lin, "The characteristic impedance of the stripline and microstrip line of the elliptic cone," *Microwave Opt. Technol. Lett.*, vol. 5, no. 10, pp. 506–509, Sept. 1992.
[14] V. Zargari and T. C. Rao, "Characteristic impedance of a tubular dielectric cylinder covered with conducting arc strips," *IEEE Trans. Microwave Theory Tech.*, vol. 37, pp. 1645–1647, Oct. 1989.
[15] C. Karpuz, A. Gorür, and M. Alkan, "Quasistatic analysis of cylindrical coplanar strip lines," *Microwave Opt. Technol. Lett.*, vol. 17, no. 2, pp. 148–151, Feb. 1998.
[16] W. Hilberg, "From approximations to exact relations for characteristic impedance," *IEEE Trans. Microwave Theory Tech.*, vol. MTT-17, pp. 259–265, May 1969.

Power and Noise Limitations of Active Circulators

Geert Carchon and Bart Nauwelaers

***Abstract*—In this paper, new simple formulas expressing the power and noise limitations for three three-way circulator architectures and three quasi-circulator architectures are derived. It is shown that the power-handling capability of the active three-way circulators is determined by the required transconductance of the transistors in the circuit, while the noise is determined by the drain noise current source. The suitability of the different active circulator architectures for transmit/receive applications is investigated. We conclude that the quasi-circulators based on passive isolation offer the highest performance.**

***Index Terms*—Active circulator, MMIC, noise.**

I. Introduction

Circulators are important components in many microwave systems [1], e.g., for the separation of transmitted and received signals. They are usually fabricated with passive nonreciprocal ferrite materials. An alternative is to use the nonreciprocal behavior of transistors. These active circulators [1]–[8] offer the advantage of small size and weight, low cost, and full compatibility with monolithic-microwave integrated-circuit (MMIC) technology. However, they also introduce excess noise and limit the RF power-handling capability.

In Section II, new simple formulas expressing the power and noise limitations of active three-way circulators and active quasi-circulators are derived. In Section III, the suitability of the different architectures for transmit–receive (Tx/Rx) applications is investigated by comparing their power-to-noise ratios.

II. Power and Noise Properties of Active Circulators

We will make a distinction between active three-way circulators and active quasi-circulators [5]: active three-way circulators exhibit full rotational symmetry and should be realized with some loss for stability reasons. Active quasi-circulators on the other hand, do not pass the signal from the receiver to the transmitter side and can be realized with gain on transmit and receive.

TABLE I
Meaning of the Symbols Used in the Calculations

NF	noise figure
r_{ds}^{TOR}	drain-source resistance of the transistors
g_m^{TOR}	Transconductance of the transistors
V_{gs}^{max}	maximum gate-source voltage
Z_{in}	input impedance of the circulator
V_{ds}^{max}	maximum drain-source voltage
Z_{opt}	optimal load-impedance for the MPA
F_{LNA}	noise figure of the LNA used in the receiver
i_g	gate noise-current source of the transistor
i_d	drain noise-current source of the transistor

It is our intension to compare the performance of active three-way circulators and active quasi-circulators for Tx/Rx applications. As active quasi-circulators are realized with gain on receive and three-way circulators are not, it is necessary to calculate the noise figure (NF) of the receiver. For simplicity, we assume that the NF of the receiver can be approximated by the contribution of the circulator and the low-noise amplifier (LNA).

The isolation between transmitter and receiver is assumed to be perfect. Therefore, the transmitter will not influence the NF of the receiver.

The explanation of the symbols used in the derivation of the power and noise properties, is given in Table I. In the following, the transmitter will always be located at port 1, the antenna at port 2, and the receiver at port 3.

A. Active Three-Way Circulators

We distinguish the architecture of Tanaka [2], the THRU-element circulator [1], and the architecture of Katzin [4]. The lossless limit of these architectures will be analyzed.

As will be shown below, the full g_m potential of the transistor is often not required in the design of active three-way circulators. In these cases, an artificial g_m reduction is obtained with a capacitor in series with the gate since only a fraction of the input power appears over the gate–source junction. This will also increase the power handling capability as the gate–source voltage swing is the power-limiting factor.

1) Principle of Tanaka: The architecture is given in Fig. 1(a). If the transistors are modeled with g_m only, it was shown in [9] that a lossless realization matched to 50 Ω requires $Z_D = Z = \infty$, $g_m = 40$mS, and $Z_{\rm RC} = 150\,\Omega$. The power can be limited by the maximum allowed $V_{\rm gs}$ and $V_{\rm ds}$ swing. $V_{\rm gs}$ is maximal over transistor T_2, while $V_{\rm ds}$ is maximal over transistor T_3. The limiting voltages are then $V_{\rm gs}^{T2} = 2/3V_{\rm in}$ and $V_{\rm ds}^{T3} = 2/3V_{\rm in}$. If $g_m^{\rm TOR} > g_m^{\rm Target}$, we can put a capacitor in series with the gate. If the impedance at port 1 is given by $Z_{\rm in}$, the maximum output power is given by

$$P_{\max} = \left(\frac{3}{2}\min\left\{\frac{g_m^{\rm TOR}}{40\text{ mS}}V_{\rm gs}^{\max}; V_{\rm ds}^{\max}\right\}\right)^2 \Big/ 2Z_{\rm in}. \qquad (1)$$

The gate and drain noise current sources of the transistor (represented by I_1, I_2, and I_3) and resistor $Z, Z_{\rm RC}, Z_D$ [see Fig. 1(a)] contribute to the NF.

The presence of the high power amplifier (HPA) will not influence the NF of the circulator, as the transmitter is assumed to be perfectly

Manuscript received November 23, 1998. This work was supported by the Flemish Institute for the Advancement of Scientific–Technological Research in Industry under a scholarship.
The authors are with the ESAT-TELEMIC Division, Katholieke Universiteit Leuven, B-3001 Heverlee, Belgium (e-mail: geert.carchon@esat.kuleuven.ac.be).
Publisher Item Identifier S 0018-9480(00)00862-0.

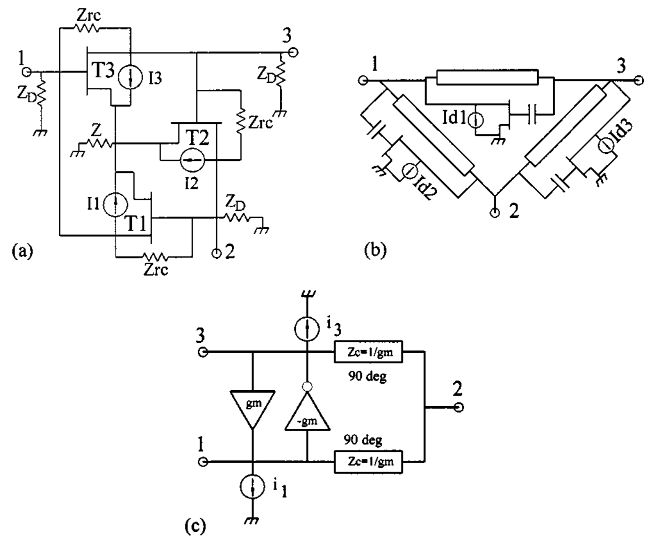

Fig. 1. Investigated three-way circulators. (a) Architecture of Tanaka. (b) THRU-element circulator. (c) Principle of Katzin.

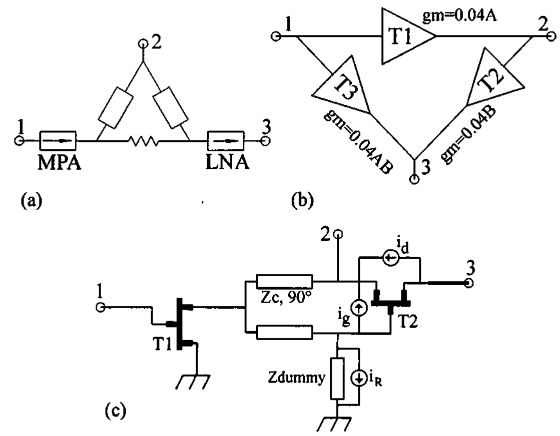

Fig. 2. Investigated quasi-circulators. (a) Architecture based on passive isolation. (b) Phase cancellation concept of Cryan. (c) Divider/combiner concept of Gasmi.

isolated from the receiver. After some calculations, we find that the NF of the circulator is given by

$$\mathrm{NF} = 1 + \frac{2}{3} + \frac{50\,\Omega}{4kT_0B}\left[\frac{2}{3}(\overline{|i_d|^2} + \overline{|i_g|^2}) + 2\,\mathrm{Re}\,(\overline{i_d^* i_g})\right]. \qquad (2)$$

The term $2/3$ is due to the contribution of Z_{RC}. In a first approximation, the gate noise current source and correlation can be neglected as they are much smaller then $\overline{|i_d|^2}$ [10]. We then obtain the following overall NF:

$$\mathrm{NF} = 1 + \frac{2}{3} + \frac{50\,\Omega}{6kT_0B}\overline{|i_d|^2} + (F_{\mathrm{LNA}} - 1). \qquad (3)$$

2) THRU-Element Circulator : The architecture consists of three identical building blocks (THRU elements) interconnected in a Δ shape [see Fig. 1(b)]. A transistor in parallel with a transmission line is the THRU element.

To determine the power-handling capability of the circulator, the required transconductance of the transistors has to be calculated. The desired S-matrix of the circulator (S_D) is given in (4). The equivalent Y-matrix representation is referred to as Y_D.

$$S_D = \begin{bmatrix} 0 & 0 & x \\ x & 0 & 0 \\ 0 & x & 0 \end{bmatrix}, \qquad \text{with } x = \alpha e^{j\varphi} \qquad (4)$$

The circulator's Y-matrix (Y_T) can also be expressed in terms of the Y-parameters of the THRU element. Equating Y_T with Y_D gives the following conditions:

$$\begin{aligned} Y_{11}^{\mathrm{THRU}} + Y_{12}^{\mathrm{THRU}} &= \frac{1 - x^3}{50(1 + x^3)} \\ Y_{12}^{\mathrm{THRU}} &= \frac{2x^2}{50(1 + x^3)} \\ Y_{21}^{\mathrm{THRU}} &= \frac{-2x}{50(1 + x^3)} \\ \text{with } Y_{ij}^{\mathrm{THRU}} &= Y_{ij}^{\mathrm{TOR}} + Y_{ij}^{\mathrm{Line}}. \end{aligned} \qquad (5)$$

For a lossless realization, the first condition is purely imaginary. For the combination of a transistor with infinite $r_{\mathrm{ds}}^{\mathrm{TOR}}$ and a lossless line, it can be met by adding shunt stubs at the ports. The second and third condition determine the transistor's g_m and line properties.

As Y_{12}^{TOR} and $\mathrm{Re}(Y_{12}^{\mathrm{Line}}) = 0$, we should define (α, φ) such that $\mathrm{Re}(Y_{12}^{\mathrm{THRU}}) = 0$. For the other transistor orientation $Y_{21}^{\mathrm{TOR}} = 0$, we then set $\mathrm{Re}(Y_{21}^{\mathrm{THRU}}) = 0$. For a given loss α, φ can now be calculated. A lossless solution cannot be found, but as $\alpha \to 1$, $g_m \to 1/75$S. The power-handling capability is then given by

$$P_{\max} = \alpha^2 \left(\min\left\{\frac{g_m^{\mathrm{TOR}} V_{\mathrm{gs}}^{\max}}{\frac{1}{75}\ \mathrm{S}}; V_{\mathrm{ds}}^{\max}\right\}\right)^2 \Big/ 2Z_{\mathrm{in}}. \qquad (6)$$

The NF is dominated by the drain noise current source of the transistors, as they are directly located at the antenna and receiver ports: I_{d1} does not influence the NF, while for a lossless realization, I_{d2} and I_{d3} have an identical noise contribution. If we again neglect the gate noise current source and correlation (because they are much smaller then $\overline{|i_d|^2}$ [10]), we obtain the following overall NF:

$$\mathrm{NF} = 1 + \frac{50\,\Omega}{4kT_0B}\overline{|i_d|^2}\left(1 + \frac{1}{\alpha^2}\right) + \frac{F_{\mathrm{LNA}} - 1}{\alpha^2}. \qquad (7)$$

3) Narrow-Band Circulator of Katzin : The architecture consists of an inverting and a noninverting amplifier in parallel, together with two 90° transmission lines [see Fig. 1(c)]. For a transistor with infinite $r_{\mathrm{ds}}^{\mathrm{TOR}}$, it was shown that a lossless realization matched to 50 Ω requires $g_m = 20$ mS and $Z_c = 50\,\Omega$. For narrow-band operation, the noninverting amplifier can be realized by cascading a common-source transistor and a 180° transmission line.

The power-handling capability is limited by $V_{\mathrm{gs}}^{\max}$ of the noninverting amplifier. The dynamic load line of the noninverting amplifier is a vertical line since the receiver is isolated from the transmitter ($V_{\mathrm{sweep}}^{\mathrm{isolatedport}} = 0$ or $Z_{\mathrm{load}} = 0$). $P_{\max}$ is, therefore, given by

$$P_{\max} = \left(\min\left\{\frac{g_m^{\mathrm{TOR}}}{20\ \mathrm{mS}} V_{\mathrm{gs}}^{\max}; V_{\mathrm{ds}}^{\max}\right\}\right)^2 \Big/ 2Z_{\mathrm{in}}. \qquad (8)$$

The noise sources can be represented by i_1 and i_3

$$\begin{aligned} i_1 &= i_d^{\text{invertor}} + i_g^{\text{non-invertor}} \\ i_3 &= i_d^{\text{non-invertor}} + i_g^{\text{invertor}}. \end{aligned} \qquad (9)$$

If we neglect i_g^{invertor} and the correlation, we obtain

$$\mathrm{NF} = 1 + \frac{50\,\Omega}{4kT_0B}\overline{|i_d^{\text{non-invertor}}|^2} + (F_{\mathrm{LNA}} - 1). \qquad (10)$$

The NF is dominated by $i_d^{\text{non-invertor}}$. Noise current source i_1 does not influence the NF of the circulator.

B. Active Quasi-Circulators

In this section, we distinguish quasi-circulators based on passive isolation, the phase-cancellation concept of Cryan [8], and the divider/combiner concept [3].

1) Quasi-Circulator Based on Passive Isolation: A passive device (e.g., a Wilkinson, etc.) is used to provide the isolation between transmitter and receiver. The architecture based on a Wilkinson divider is given in Fig. 2(a).

The power-handling capability and NF are given by

$$P_{\max} = (V_{\rm ds}^{\max})^2 / 4 \cdot Z_{\rm opt} \tag{11}$$

and

$$\mathrm{NF} = 2F_{\rm LNA}. \tag{12}$$

2) Phase-Cancellation Concept of Cryan : The output power of this architecture is limited by $V_{\rm gs}^{\max}$ of transistor T_2 [see Fig. 2(b)]. A series capacitor can be used to increase the power handling capability, but this reduces the gain on receive. The maximum output power is given by

$$P_{\max} = \left(V_{\rm gs}^{\max}\right)^2 / 2 \cdot Z_{\rm in}. \tag{13}$$

If we neglect the influence of i_g^{T2} (small compared to i_d^{T1}) and i_d^{T2}, i_d^{T3}(the signal has already been amplified), the NF is given by

$$\mathrm{NF} = 1 + \frac{50\,\Omega}{4kT_0B}\overline{|i_d^{T1}|^2} + (F_{\rm LNA} - 1). \tag{14}$$

3) Divider/Combiner Concept: Many divider/combiner combinations are possible (in-phase, out-of-phase, passive, active) [5]–[7]. Only the combination presented in [7] is analyzed [see Fig. 2(c)]. For all other divider–combiner combinations found in literature, either the output power is very low or the noise of the HPA affects the NF of the receiver. This architecture consists of a passive in-phase divider and an active out-of-phase combiner.

Half of the output power of transistor $T1$ is dissipated in the 50-Ω dummy load. The output power is also limited by the maximum drain–source voltage swing of the out-of-phase combiner (transistor $T2$). This is given by

$$P_{\max} = (V_{\rm ds}^{\max})^2 / 2 \cdot Z_{\rm in}. \tag{15}$$

Transistor $T1$ does not contribute to the NF if perfect isolation is assumed [7]. If the transistors are modeled with their g_m only, the NF becomes

$$\mathrm{NF} = 1 + \frac{50\,\Omega}{4kT_0}\left\{\overline{|i_R|^2} + 4\overline{|i_g|^2} + \frac{\overline{|i_d|^2}}{(g_mZ_c)^2} - \frac{4\,\mathrm{Re}\{\overline{i_g^* i_d}\}}{g_mZ_c}\right\}. \tag{16}$$

The noise contribution of the dummy load is 3 dB. An ideal noise match cannot be guaranteed with this simple architecture. This can be improved by adding additional matching elements, hereby complicating the architecture.

III. Discussion

Using the above derived formulas, the suitability of the different circulator architectures for Tx/Rx applications can be investigated. The ratio $P_{\max}/\mathrm{NF}_{\rm receiver}$ will be used as comparison criterion [11]. Each type will be compared with the Wilkinson-based quasi-circulator, as this is the best performance that can be achieved by using a passive reciprocal device to provide the necessary Tx/Rx isolation.

A. Active Three-Way Circulators

The power-handling capability can be increased by choosing a transistor with a larger g_m or, equivalently, a larger gatewidth. This can be done as long as the output power is not limited by $V_{\rm ds}^{\max}$. The NF is each time determined by $\overline{|i_d|^2}$. The power-handling capability and noise performance cannot be optimized separately, as both parameters are related by

$$\overline{i_d^2} = 4kTg_mP \tag{17}$$

where P is a dimensionless parameter within the range of 1–3, depending upon the technological parameters and biasing conditions [10].

Both g_m and $\overline{|i_d|^2}$ linearly scale as a function of gatewidth. The power-to-noise ratio, therefore, improves by choosing a larger transistor up to a point where the power is limited by $V_{\rm ds}^{\max}$.

As a practical example, we take the following parameters: $V_{\rm gs}^{\max} = 0.3$ V, $V_{\rm ds}^{\max} = 3$ V, $g_m^{\rm TOR} = 50$ mS, and $i_d = 34$ pA (typical values for a 2 × 60 µm transistor, biased at 50% $I_{\rm dss}$ and $V_{\rm ds} = 3$ V from the H40 process of GEC-Marconi, Caswell, U.K.) [12].

The maximum power handling capability is then 23 dBm for the concept of Tanaka, 19.5 dBm for the THRU-element circulator and 19.5 dBm for the concept of Katzin. If $F_{\rm LNA} = 3$ dB, the corresponding overall NF becomes, respectively, 13, 12.9, and 11.8 dB. This gives $P_{\max}/\mathrm{NF} = 10, 6.5$, and 7.7 dBm. If the same output power was delivered by the (medium power amplifier (MPA) in the Wilkinson-based quasi-circulator, we would get 14, 10.5, and 10.5 dBm, respectively.

Thus, we conclude that the lossless realization of the active three-way circulators does not compensate for the larger NF and that the overall performance is inferior to a Wilkinson-based quasi-circulator. In practice, the lossless realization will not be possible due to the finite $r_{\rm ds}$, such that the overall performance will be even worse.

B. Phase-Cancellation Concept of Cryan

The output power is very limited as $V_{\rm gs}^{\max} \ll V_{\rm ds}^{\max}$. The NF is large as it is determined by i_d^{T1}. It is, therefore, not very well suited for Tx/Rx applications.

C. Divider/Combiner Concept of Gasmi

The Wilkinson-based quasi-circulator and the divider/combiner concept dissipate half of the output power. The output power of the Wilkinson-based quasi-circulator can be increased by using power-combining networks at the transmitter side. This cannot be done for the divider/combiner concept, as the power is limited by the maximum drain–source voltage swing of the combiner. Additionally, to improve the NF, transistor $T2$ is usually biased at $V_{\rm ds} < V_{\rm ds}^{\rm breakdown}/2$, hereby further limiting the maximum output power (this is, e.g., the case for InP technologies, where $V_{\rm ds} = 1$ V is typical for low-noise biasing). The Wilkinson-based quasi-circulator, therefore, has a higher maximum output power.

For equal output powers, the possible gain of the divider/combiner concept has to come from an improved NF. This is, however, not obvious as it is not possible to bias transistor $T2$ at low drain–source voltages if a large output power is required. In practice, part of the input power will leak to the HPA, which further lowers the gain on receive and increases the NF. Additionally, transistors with only one source connection are to be used for layout purposes. This increases $\mathrm{NF}_{\min}$ and decreases the associated gain of the transistors. Finally, an optimal noise match cannot be guaranteed with the architecture in Fig. 2(c). The latter can be seen in [7], where a $\mathrm{NF} = 5.3$ dB with 4 dB gain was simulated at 4 GHz (for this transistor, (16) predicts $\mathrm{NF} = 5$ dB). If this transistor ($\mathrm{NF}_{\min} = 1$ dB with 11.6 dB associated gain) was used in a Wilkinson-based quasi-circulator, an overall $\mathrm{NF} = 4$ dB seems possible.

From the previous considerations, we conclude that the overall power-to-noise performance of the Wilkinson-based quasi-circulator is superior to the divider/combiner concept.

IV. CONCLUSION

Simple formulas expressing the power and noise limitations for three three-way and three quasi-circulator architectures are derived. It is shown that the power-handling capability of the active three-way circulators is determined by the required g_m of the transistors in the circuit while the noise is determined by the drain noise current source. We conclude that active three-way circulators are not the optimal choice for Tx/Rx applications because the theoretical lossless realization does not compensate for the rather large NF. The best architectures are the divider/combiner concept of Gasmi and the Wilkinson-based quasi-circulator, with preference for the latter.

REFERENCES

[1] Y. Ayasli, “Field effect transistor circulators,” *IEEE Trans. Magn.*, vol. 25, pp. 3242–3247, May 1989.

[2] S. Tanaka, N. Shimomura, and K. Ohtake, “Active circulators—The realization of circulators using transistors,” *Proc. IEEE* , vol. 53, pp. 260–267, Mar. 1965.

[3] S. Hara, T. Tokumitsu, and M. Aikawa, “Novel unilateral circuits for MMIC circulators,” *IEEE Trans. Microwave Theory Tech.*, vol. 38, pp. 1399–1406, Oct. 1990.

[4] P. Katzin, Y. Ayasli, L. Reynolds, and B. Bedard, “6 to 18 GHz MMIC circulators,” *Microwave J.*, pp. 248–256, May 1992.

[5] D. Köther, B. Hopf, T. Sporkmann, and I. Wolff, “Active CPW MMIC circulators for the 40 GHz band,” in *European Microwave Conf.*, Cannes, France, 1994, pp. 542–547.

[6] D. Köther, B. Hopf, T. Sporkmann, I. Wolff, and S. Kosslowski, “New types of MMIC circulators,” in *IEEE MTT-S Int. Microwave Symp. Dig.* Orlando, FL, 1995, pp. 877–880.

[7] A. Gasmi, B. Huyart, E. Bergeault, and L. Jallet, “Noise and power optimization of a MMIC quasi-circulator,” *IEEE Trans. Microwave Theory Tech.*, vol. 45, pp. 1572–1577, Sept. 1997.

[8] M. J. Cryan and P. S. Hall, “An integrated active circulator antenna,” *IEEE Microwave Guided Wave Lett.*, vol. 7, pp. 190–191, July 1997.

[9] A. Gasmi, “Conception et réalization de circulateurs actifs microondes en technologie monolithique MMIC: Calcul des paramètres de bruit des transistors pour l'optimization des performances en bruit des circulateurs,” Ph.D. dissertation, Dept. Electron. Commun., Ecole Nationale Supérieure Télecommun., Paris, France, 1997.

[10] A. Cappy, “Noise modeling and measurement techniques,” *IEEE Trans. Microwave Theory Tech.*, vol. 36, pp. 1–10, Jan. 1988.

[11] D. K. Barton, *Modern Radar System Analysis Vol. I*, 1st ed. Norwood, MA: Artech House, 1988.

[12] *H40 Design Manual*, GEC-Marconi, Caswell, U.K..

Analysis of Elliptical Waveguides by Differential Quadrature Method

C. Shu

***Abstract*—A new approach for elliptical waveguide analysis is presented in this paper. This approach applies the global method of a differential quadrature (DQ) to discretize the Helmholtz equation and then reduces it into an eigenvalue equation system. All the cutoff wavelengths from low- to high-order modes can be simultaneously obtained from the eigenvalues of the equation system. The present solver is general, which can be applied to elliptical waveguides with arbitrary ellipticity. It is demonstrated in this paper that the DQ results are in excellent agreement with theoretical values using just a few grid points and, thus, requiring very small computational effort.**

***Index Terms*—Eigenvalues, elliptical waveguides, generalized differential quadrature, global method, waveguide analysis, wavelength.**

I. INTRODUCTION

Elliptical waveguides have been extensively used in many engineering problems such as radar feed lines, multichannel communication, and accelerator beam tubes. The determination of the cutoff wavelength of elliptical waveguides is one of the important issues for designing the waveguide or analyzing the wave propagation in the waveguide. The analysis of elliptical waveguides has been studied by several researchers. In 1938, Chu [1] first presented the theory of the transmission of the electromagnetic waves in an elliptical waveguide. Since then, subsequent results about the cutoff wavelengths have been reported in [2]–[5]. Most of these results are from computing the zeros of the modified Mathieu functions of the first kind. However, it is not convenient to determine the eigenmode sequence of an elliptical waveguide with given ellipticity for such computations since a large number of calculations are required. In addition, the high-order modes in eigenmode sequence may be missed during the computation. Thus, we need a more direct and convenient way to compute the cutoff wavelengths for a given elliptical waveguide.

As will be shown in this paper, the global method of differential quadrature (DQ) offers a promising way to determine the cutoff wavelengths of elliptical waveguides. The accurate numerical results can be obtained by using a considerably small number of grid points. The DQ method was first proposed by Bellman *et al.* [6] and then improved by Shu [7] and Shu and Chew [8] in computing the weighting coefficients. Thus far, the DQ-type methods have been successfully applied to solve flow problems [7]–[9] and structural and vibration problems [10]–[11] with high efficiency. This paper will show the detailed implementation and application of the DQ method in the elliptical waveguide analysis.

II. DQ METHOD

For simplicity, the one-dimensional problem is chosen to demonstrate the DQ method. Following the idea of an integral quadrature, it is assumed that any derivative at a grid point is approximated by a linear

Manuscript received August 31, 1999.

The author is with the Department of Mechanical and Production Engineering, National University of Singapore, Singapore 119260.

Publisher Item Identifier S 0018-9480(00)00861-9.

summation of all the functional values in the whole computational domain. For example, the first- and second-order derivatives of $f(x)$ at a point x_i are approximated by

$$f_x(x_i) = \sum_{j=1}^{N} a_{ij} \cdot f(x_j), \qquad \text{for } i = 1, 2, \cdots, N, \tag{1}$$

$$f_{xx}(x_i) = \sum_{j=1}^{N} b_{ij} \cdot f(x_j), \qquad \text{for } i = 1, 2, \cdots, N, \tag{2}$$

where N is the number of grid points, and a_{ij},b_{ij} are the weighting coefficients, f_x,f_{xx} represent the first- and second-order derivatives of the function $f(x)$. The determination of weighting coefficients a_{ij} and b_{ij} depends on how to approximate the function $f(x)$. It has been shown by Shu [7] that when $f(x)$ is approximated by a high-order polynomial with the form

$$f(x) = \sum_{k=1}^{N} c_k \cdot x^{k-1} \tag{3}$$

where c_k are constants, the weighting coefficients a_{ij} and b_{ij} can be computed by the following explicit formulations:

$$a_{ij} = \frac{P(x_i)}{(x_i - x_j) \cdot P(x_j)}, \qquad \text{for } j \neq i \tag{4a}$$

$$a_{ii} = -\sum_{j=1, j\neq i}^{N} a_{ij} \tag{4b}$$

$$b_{ij} = 2a_{ij} \left(\cdot a_{ii} - \frac{1}{x_i - x_j} \right), \qquad \text{for } j \neq i \tag{5a}$$

$$b_{ii} = -\sum_{j=1, j\neq i}^{N} b_{ij} \tag{5b}$$

where

$$P(x_k) = \prod_{j=1, j\neq k}^{N} (x_k - x_j).$$

Since (4) and (5) are based on the polynomial approximation, for simplicity, they are noted as the polynomial differential quadrature (PDQ).

For some problems, especially those with periodic behaviors, the polynomial approximation may not be the best fitting. In contrast, the Fourier series expansion can provide more accurate results. It has been shown by Shu and Chew [8] that when $f(x)$ is approximated by a truncated Fourier series expansion with the form

$$f(x) = c_0 + \sum_{k=1}^{N/2} (c_k \cos kx + d_k \sin kx) \tag{6}$$

where c_k, d_k are constants, the weighting coefficients a_{ij}, b_{ij} can be computed by

$$a_{ij} = \frac{1}{2} \cdot \frac{F(x_i)}{F(x_j) \cdot \sin \dfrac{x_i - x_j}{2}}, \qquad \text{when } j \neq i \tag{7a}$$

$$a_{ii} = -\sum_{j=1, j\neq i}^{N} a_{ij} \tag{7b}$$

$$b_{ij} = a_{ij} \left[2a_{ii} - ctg \frac{x_i - x_j}{2} \right], \qquad \text{when } j \neq i \tag{8a}$$

$$b_{ii} = -\sum_{j=1, j\neq i}^{N} b_{ij} \tag{8b}$$

where

$$F(x_i) = \prod_{k=1, k\neq i}^{N} \sin(x_i - x_k/2).$$

Equations (7) and (8) are based on the Fourier series expansion, which can be noticed as the Fourier differential quadrature (FDQ) approach. It is indicated that (4) and (5) and (7) and (8) are derived from the analysis of a linear vector space. For details, see [7] and [8]. It is also noted that PDQ and FDQ use the same formulations to discretize the derivatives. The difference of these two approaches is on the computation of weighting coefficients. When (7) and (8) are applied to a periodic problem, the periodic condition is automatically satisfied in the FDQ discretization. Thus, the implementation of periodic condition is not needed in the FDQ approach.

III. Governing Equations and Numerical Algorithms

Electromagnetic waves propagating in the elliptical waveguide are the combination of the TM and TE waves. For the TM waves, the longitudinal components of the waves are $H_z = 0$, $E_z = \phi$, while for the TE waves, $H_z = \phi$ and $E_z = 0$. Here, ϕ is the general solution of following Helmholtz equation:

$$\nabla^2 \phi + k_c^2 \phi = 0 \tag{9}$$

where ∇^2 is the Laplacian operator given by

$$\nabla^2 = \frac{\partial^2}{\partial x^2} + \frac{\partial^2}{\partial y^2} \tag{10}$$

and k_c is the cutoff wavenumber. The TE waves satisfy the Neumann boundary condition as follows:

$$\left.\frac{\partial \phi}{\partial n}\right|_{\partial D} = \left.\frac{\partial H_z}{\partial n}\right|_{\partial D} = 0 \tag{11}$$

while the TM waves meet the Dirichlet boundary condition

$$\phi|_{\partial D} = E_z|_{\partial D} = 0 \tag{12}$$

where ∂D is the boundary of elliptical waveguide cross section, which can be given by the following equation:

$$(x/a)^2 + (y/b)^2 = 1. \tag{13}$$

Here, a and b are semimajor and semiminor axes, respectively.

Like the classical finite-difference methods, the DQ approach requires the computational domain to be rectangular. To meet this, we can use the following transformation:

$$\begin{cases} x = ar \cdot \cos\theta \\ y = br \cdot \sin\theta. \end{cases} \tag{14}$$

With (14), the computational domain becomes a rectangle with $0 \leq r \leq 1, 0 \leq \theta \leq 2\pi$. It is noted that the boundary of the elliptical cross section is now represented by $r = 1$. $r = 0$ represents the center of the cross section.

With (14), (9) can be transformed accordingly into

$$A\frac{\partial^2 \phi}{\partial r^2} + \frac{B}{r} \cdot \frac{\partial^2 \phi}{\partial r \partial \theta} + \frac{C}{r^2} \cdot \frac{\partial^2 \phi}{\partial \theta^2} + \frac{C}{r} \cdot \frac{\partial \phi}{\partial r} - \frac{B}{r^2} \cdot \frac{\partial \phi}{\partial \theta} + a^2 k_c^2 \phi = 0 \tag{15}$$

where $A = \lambda^2 \cdot \sin^2\theta + \cos^2\theta$, $B = (\lambda^2 - 1)\sin 2\theta$, $C = \lambda^2 \cdot \cos^2\theta + \sin^2\theta$, $\lambda = a/b$. Equation (15) will be used to determine the wavenumber k_c. For the TM waves, the boundary condition at $r = 1$ is the same as given by (12), i.e., $\phi = 0$ at $r = 1$. For the TE waves, the

Neumann condition given by (11) can be written in the (r, θ) coordinate system as

$$A\frac{\partial \phi}{\partial r} + \frac{B}{2}\frac{\partial \phi}{\partial \theta} = 0, \qquad \text{at } r = 1. \tag{16}$$

In addition, (15) needs a boundary condition at $r = 0$. This can be given from the consistent condition of (15) at $r = 0$, which can be written as

$$\frac{\partial \phi}{\partial r} = 0, \qquad \text{at } r = 0. \tag{17}$$

Equation (17) will be applied to both the TM and TE waves. In the θ direction, the periodic condition is applied.

In this study, the derivatives in the r-direction are discretized by the PDQ approach while the derivatives in the θ-direction are approximated by the FDQ approach. It is supposed that there are N grid points in the r-direction and M grid points in the θ-direction. Using the DQ method, (15) can be discretized at a mesh point (r_i, θ_j) as

$$\begin{aligned}\sum_{k=1}^{N}\left(A_j b_{i,k} + \frac{C_j}{r_i}a_{i,k}\right)\cdot \phi_{k,j} \\ + \frac{B_j}{r_i}\cdot\sum_{k1=1}^{N}\sum_{k2=1}^{M} a_{i,k1}\cdot \overline{a}_{j,k2}\cdot\phi_{k1,k2} \\ + \sum_{k=1}^{M}\left(\frac{C_j}{r_i^2}\overline{b}_{j,k} - \frac{B_j}{r_i^2}\overline{a}_{j,k}\right)\cdot\phi_{i,k} + a^2k_c^2\phi_{i,j} = 0\end{aligned} \tag{18}$$

where $a_{i,k}, b_{i,k}$ are the weighting coefficients of the derivatives $\partial\phi/\partial r, \partial^2\phi/\partial r^2$ computed by (4) and (5) while $\overline{a}_{j,k}, \overline{b}_{j,k}$ are the weighting coefficients of the derivatives $\partial\phi/\partial\theta, \partial^2\phi/\partial\theta^2$, computed by (7) and (8). It is indicated that (18) has to be applied at the interior points $2 \le i \le N-1, 1 \le j \le M$. Similarly, the derivatives in the boundary conditions can be discretized by the DQ method. In the θ-direction, no numerical condition is implemented since the periodic condition is automatically satisfied in the FDQ discretization. It is supposed that the function values at interior points are represented by a vector $\{\phi_I\}$, and the remaining function values at the boundary points are denoted by a vector $\{\phi_B\}$. With these definitions, equation system (18) can be written as the following matrix form:

$$[A_{IB}]\cdot\{\phi_B\} + [A_{II}]\cdot\{\phi_I\} = \Omega^2\cdot\{\phi_I\} \tag{19}$$

where $\Omega^2 = a^2k_c^2$. Similarly, the discretized boundary conditions can be put in the following matrix form:

$$[A_{BB}]\cdot\{\phi_B\} + [A_{BI}]\cdot\{\phi_I\} = 0. \tag{20}$$

Substituting (20) into (19) gives the eigenvalue equation system as

$$\left\{[A_{II}] - [A_{IB}]\cdot[A_{BB}]^{-1}\cdot[A_{BI}]\right\}\cdot\{\phi_I\} = \Omega^2\cdot\{\phi_I\}. \tag{21}$$

Once the eigenvalue of above system Ω is computed, the cutoff wavenumber k_c can easily be obtained.

IV. Results and Discussion

As shown in [7], the use of nonuniform mesh in the PDQ discretization would give a more stable numerical solution. Thus, the following nonuniform mesh is used in the r-direction [7]:

$$r_i = \frac{1}{2}\left[1 - \cos\left(\frac{i-1}{N-1}\cdot\pi\right)\right], \qquad i = 1, 2, \cdots, N. \tag{22}$$

The use of FDQ approach in the θ-direction requires the following uniform mesh:

$$\theta_j = \frac{j-1}{M}2\pi, \qquad j = 1, 2, \cdots, M. \tag{23}$$

To validate the efficiency of the DQ method, the normalized cutoff wavelength defined by $\lambda_c = 2\pi/k_c$ is computed and compared with analytical solution for two eccentricities. Tables I–II show the normalized wavelengths of the first nine TM modes for eccentricity of 0.1, 0.9 while Tables III–IV list the normalized wavelengths of the first nine TE modes for eccentricity of 0.1, 0.9. Also included in these tables are the analytical solutions given by Zhang and Shen [5]. It is noted that for each table, five mesh sizes are used to obtain the DQ results. It can be observed from the tables that for both the TM and TE modes, the convergence of the DQ results is very obvious. When the mesh size is slightly increased, the accuracy of the DQ results is greatly improved. It can also be seen from the tables that the convergence of the DQ results for the TM modes is faster than that for the TE modes. In other words, to obtain a grid-independent DQ result, the TM modes require less mesh points than the TE modes.

Table I shows that when e (eccentricity) $= 0.1$, the normalized cutoff wavelengths of the first nine TM modes computed by the DQ method

TABLE I
Normalized Cutoff Wavelengths of First Nine TM Modes ($e = 0.1$)

Modes	Analytical [5]	*DQ Results*				
		11×7	15×7	18×7	21×7	18×5
TM_1	2.6062	2.6062	2.6062	2.6062	2.6062	2.6062
TM_2	1.6377	1.6379	1.6378	1.6377	1.6377	1.6377
TM_3	1.6336	1.6338	1.6337	1.6336	1.6336	1.6336
TM_4	1.2204	1.2204	1.2204	1.2204	1.2204	1.2204
TM_5	1.2204	1.2204	1.2204	1.2204	1.2204	1.2204
TM_6	1.1353	1.1353	1.1353	1.1353	1.1353	1.1353
TM_7	0.9823	0.9823	0.9823	0.9823	0.9823	-
TM_8	0.9823	0.9823	0.9823	0.9823	0.9823	-
TM_9	0.8945	0.8946	0.8945	0.8945	0.8945	0.8945

TABLE II
Normalized Cutoff Wavelengths of First Nine TM Modes ($e = 0.9$)

Modes	Analytical [5]	*DQ Results*				
		9×19	13×19	14×19	17×19	14×17
TM_1	1.4906	1.4906	1.4906	1.4906	1.4906	1.4906
TM_2	1.1607	1.1610	1.1608	1.1607	1.1607	1.1607
TM_3	0.9375	0.9375	0.9375	0.9375	0.9375	0.9375
TM_4	0.8093	0.8096	0.8094	0.8093	0.8093	0.8093
TM_5	0.7803	0.7804	0.7803	0.7803	0.7803	0.7803
TM_6	0.7083	0.7083	0.7083	0.7083	0.7083	0.7083
TM_7	0.6651	0.6651	0.6651	0.6651	0.6651	0.6651
TM_8	0.6262	0.6262	0.6262	0.6262	0.6262	0.6262
TM_9	0.5780	0.5786	0.5780	0.5780	0.5780	0.5778

TABLE III
Normalized Cutoff Wavelengths of First Nine TE Modes ($e = 0.1$)

Modes	Analytical [5]	*DQ Results*				
		9×9	11×9	12×9	31×9	12×7
TE_1	3.4119	3.3913	3.3985	3.4233	3.4104	3.4233
TE_2	3.3962	3.3757	3.3829	3.4075	3.3947	3.4075
TE_3	2.0521	2.0521	2.0521	2.0521	2.0521	2.0521
TE_4	2.0520	2.0520	2.0520	2.0520	2.0520	2.0520
TE_5	1.6356	1.6356	1.6356	1.6356	1.6356	1.6356
TE_6	1.4918	1.4918	1.4918	1.4918	1.4918	1.4918
TE_7	1.4918	1.4918	1.4918	1.4918	1.4918	1.4918
TE_8	1.1786	1.1806	1.1792	1.1786	1.1786	1.1756
TE_9	1.1786	1.1786	1.1786	1.1786	1.1786	1.1724

TABLE IV
NORMALIZED CUTOFF WAVELENGTHS OF FIRST NINE TE MODES ($e = 0.9$)

Modes	Analytical [5]	DQ Results				
		9×19	13×19	15×19	31×19	15×17
TE_1	3.3482	3.3168	3.3340	3.3378	3.3459	3.3378
TE_2	1.8287	1.8287	1.8287	1.8287	1.8287	1.8287
TE_3	1.5650	1.5574	1.5615	1.5624	1.5644	1.5624
TE_4	1.2654	1.2687	1.2668	1.2664	1.2656	1.2664
TE_5	1.2292	1.2292	1.2292	1.2292	1.2292	1.2292
TE_6	0.9986	0.9996	0.9990	0.9989	0.9987	0.9989
TE_7	0.9698	0.9698	0.9698	0.9698	0.9698	0.9698
TE_8	0.8340	0.8340	0.8340	0.8340	0.8340	0.8342
TE_9	0.8177	0.8177	0.8177	0.8177	0.8177	0.8177

need seven grid points in the θ-direction and 18 grid points in the r-direction to match the analytical solution up to four decimal digits. When the number of grid points is above seven in the θ-direction and 18 in the r-direction, the DQ results are independent of mesh size. Thus, 18 × 7 is a minimum mesh size for a grid-independent solution of this case, although reasonable numerical solution can be provided by a smaller mesh size of 11 × 7. It is very interesting to see from Table I that when the number of grid points in the r-direction is less than 18, the accuracy of most cutoff wavelengths is reduced. However, when the number of grid points in the θ-direction is less than seven, the accuracy of computed cutoff wavelengths does not change, but some modes are lost during the computation. Another interesting phenomenon is that, as the eccentricity increases, the number of grid points required for a grid-independent solution in the θ-direction also increases. However, the minimum number of grid points in the r-direction for a grid-independent solution is slightly reduced. This can be seen from Table II. It shows that when $e = 0.9$, the grid-independent solution needs 14 grid points in the r-direction and 19 grid points in the θ-direction.

It was found that the accuracy of computed cutoff wavelengths for the TE waves is less than that for the TM waves when the same mesh size is used. This can be seen from Tables III–IV. Table III shows that when $e = 0.1$, the computed cutoff wavelengths of TE_3, TE_4, TE_5, TE_6, TE_7, TE_8, TE_9 modes can match the analytical solution up to four decimal digits by using 12 grid points in the r-direction and nine grid points in the θ-direction. However, the computed cutoff wavelengths of TE_1, TE_2 modes can only match the analytical solution up to one decimal digit. Even when the number of grid points in the r-direction is increased to 31, the computed cutoff wavelengths of TE_1, TE_2 modes just match the analytical solution up to two decimal digits. When the number of grid points in the r-direction is fixed at 12, the increase of grid points in the θ-direction above nine will not improve the accuracy of numerical solution. The above phenomenon also appears in Table IV. The convergence of computed cutoff wavelengths for the TE_3, TE_4, TE_5, TE_6, TE_7, TE_8, TE_9 modes is much faster than that for the TE_1, TE_2 modes. It was found that the slow convergence of TE_1, TE_2 modes is attributed to the numerical boundary condition imposed at the center of cross section $r = 0$. In this study, the Neumann condition is imposed at $r = 0$. With this condition, all the cutoff wavelengths can be computed in a regular sequence although the accuracy of TE_1, TE_2 modes is not so good. It was found that when a Dirichlet condition ($\phi = 0$) is imposed at $r = 0$, the accuracy of TE_1, TE_2 modes can be greatly improved. For example, when $e = 0.1$, the use of only seven grid points in the r-direction can match the computed cutoff wavelengths of TE_1 and TE_2 modes to the analytical solution up to four decimal digits. The drawback is that the cutoff wavelengths of some modes are lost in the computation. Thus, it is believed that the use of Neumann condition at $r = 0$ is more reasonable.

Since an accurate DQ solution can be obtained by using very coarse mesh, the required computational effort is extremely small. All the results shown in Tables I–IV are obtained by running the program on an IBM compatible PC Pentium 75. For all the results shown in Tables I–IV, the run time for each case is less than 2 min.

V. CONCLUSIONS

In this paper, a new approach is proposed for elliptical waveguide analysis. The present approach discretizes the Helmholtz equation by the global method of the DQ and then reduces it to a standard eigenvalue equation system. All the cutoff wavelengths can be computed simultaneously by a standard eigenvalue solver. The present solver is general, which can be applied to elliptical waveguides with arbitrary eccentricity. It was found that accurate numerical results can be obtained by the DQ method using a considerably small number of grid points. As a consequence, very small computational effort and virtual storage are needed. For all the results shown in Tables I–IV, the run time of the DQ results for a given eccentricity is less than 2 min on an IBM compatible PC Pentium 75. It was also found that the Neumann condition imposed at the center of the cross section is more reasonable than the Dirichlet condition. In summation, it can be concluded that the DQ is a very efficient method for elliptical waveguide analysis.

REFERENCES

[1] L. J. Chu, "Electromagnetic waves in elliptic hollow pipes of metal," *J. Appl. Phys.*, vol. 9, p. 583, 1938.

[2] J. G. Kretzschmar, "Wave propagation in the hollow conducting elliptical waveguide," *IEEE Trans. Microwave Theory Tech.*, vol. MTT-18, pp. 547–554, Month 1970.

[3] D. A. Goldberg, L. J. Laslett, and R. A. Rimmer, "Modes of elliptical waveguides: A correction," *IEEE Trans. Microwave Theory Tech.*, vol. 38, pp. 1603–1608, Month 1990.

[4] B. K. Wang, K. Y. Lam, M S. Leong, and P. S. Kooi, "Elliptical waveguide analysis using improved polynomial approximation," *Proc. Inst. Elect. Eng.*, vol. 141, pp. 483–488, 1994.

[5] S. J. Zhang and Y. C. Shen, "Eigenmode sequence for an elliptical waveguide with arbitrary ellipticity," *IEEE Trans. Microwave Theory Tech.*, vol. 43, pp. 227–230, Jan. 1995.

[6] R. Bellman, B. G. Kashef, and J. Casti, "Differential quadrature: A technique for the rapid solution of nonlinear partial differential equations," *J. Comput. Phys.*, vol. 10, p. 40, 1972.

[7] C. Shu, "Generalized differential-integral quadrature and applicaton to the simulation of incompressible viscous flows including parallel computation," Ph.D. dissertation, Dept. Aerospace Eng., Univ. Glasgow, Glasgow, Scotland, 1991.

[8] C. Shu and Y. T. Chew, "Fourier expansion-based differential quadrature and its application to Helmholtz eigenvalue problems," *Commun. Numer. Methods Eng.*, vol. 13, pp. 643–653, 1997.

[9] C. Shu and B. E. Richards, "Application of generalized differential quadrature to solve two-dimensional incompressible Navier–Stokes equations," *Int. J. Numer. Methods Fluids*, vol. 15, pp. 791–798, 1992.

[10] H. Du, M. K. Lim, and R. M. Lim, "Application of differential quadrature to vibration analysis," *J. Sound Vibrations*, vol. 181, p. 279, 1995.

[11] C. Shu, "Free vibration analysis of composite laminated conical shells by generalized differential quadrature," *J. Sound Vibrations*, vol. 194, p. 194, 1996.

Time-Domain Modeling of High-Speed Interconnects by Modified Method of Characteristics

Qinwei Xu, Zheng-Fan Li, Pinaki Mazumder, and Jun-Fa Mao

***Abstract*—In this paper, a new model of lossy transmission lines is presented for the time-domain simulation of high-speed interconnects. This model is based on the modified method of characteristics (MMC). The characteristic functions are first approximated by applying lower order Taylor series in the frequency domain, and then a set of simple recursive formulas are obtained in the time domain. The formulas, which involve tracking performance between two ends of a transmission line, are similar to those derived by the method of characteristics for lossless and undistorted lossy transmission lines. The algorithm, based on the proposed MMC model, can efficiently evaluate transient responses of high-speed interconnects. It only uses the quantities at two ends of the lines, requiring less computation time and less memory space than required by other methods. Examples indicate that the new method is having high accuracy and is very efficient for the time-domain simulation of interconnects in high-speed integrated circuits.**

***Index Terms*—Interconnects, modeling, modified method of characteristics, recursive calculation, transient simulation, transmission line.**

I. Introduction

In modern high-speed VLSI chips and multichip modules (MCM's), interconnects play an increasingly important role. Due to the rapid increase in operating speed and decrease in feature sizes, the electrical length of interconnects is now a significant fraction of the wavelength of signals. At high signal speeds, interconnect effects such as signal delay, reflection, dispersion, and crosstalk may deteriorate the system performance and even cause malfunction of the circuits if improperly designed [1]. Consequently, modeling of a distributed transmission line is very important for the design of a reliable high-speed integrated circuit (IC) system and accurate estimation of the system performance.

As the lossy transmission lines are traditionally modeled and analyzed in the frequency domain, well-known methods, such as the convolution technique and the fast Fourier transform (FFT), have been widely used [2], [3]. These approaches have a major difficulty when the analysis has to span a large time interval. Asymptotic waveform evaluation (AWE) [4]–[6], a moment-matching process using Padé approximation, has been shown to be an efficient technique for obtaining the approximate transient response of linear networks. However, the moment-matching process can lead to instability due to critical properties of Padé approximations, which means that it may generate right half-plane poles, albeit the systems handled are stable. Recently, the Padé moment-matching methods have been further augmented to avoid the instability [7], [8]. In the literature [7], a multipoint moment-matching technique, called complex frequency hopping (CFH), provides a new method of generating the exact poles of a linear network containing distributed and lumped elements. As a result, the instability properties of Padé approximations are bypassed and no unstable right half-plane poles are generated.

The method of characteristics (MC) is very efficient for the solution of hyperbolic partial differential equations such as the Telegrapher's equations describing transmission lines [9], [10]. The main idea of the MC is to transform the original partial differential equations into ordinary differential equations along the characteristic lines. It is well established that the MC can deal with a lossless transmission line very accurately. Also, if the transmission lines have the property $LG = RC$, which are called undistorted lines, the solutions of the Telegrapher's equations can be obtained analytically. In both cases, the MC enables circuit simulation to be very efficient, with the quantities at transmission-line ends related by closed-form formulas. In such cases, the terminal voltages and currents of the transmission line can be determined recursively in the time domain. However, if transmission lines are lossy and $LG \neq RC$, the results cannot be derived analytically. In that event, the equations should be solved numerically; the voltage and current to be computed are not limited to the two ends of the line, but various points along the line must be sampled for numerical computation [11].

However, if the transmission lines are undistorted, i.e., $LG = RC$, the solutions of the Telegrapher's equations can be obtained analytically in the time domain by the MC. Based on the analytical solution, a new algorithm named the modified method of characteristics (MMC) is presented in this paper. This method deals with lossy transmission lines with $LG \neq RC$. Lower order Taylor series is at first employed to approximate the characteristics function in the frequency domain, and then the inverse Laplace transform results in a set of recursive formulas, which describe the time-domain model of the transmission line. The recursive formulas have the form similar to those derived by MC for lossless or undistorted lossy transmission lines. As only the quantities at the ends of the lines are needed for the computation, and neither FFT nor convolution is employed, this method is expected to reduce the computation time as well as save the memory storage space.

II. MC for Transmission Line with $LG = RC$

At first, we deal with single transmission line for simplicity. Let R, L, C, and G be the resistance, inductance, capacitance, and conductance per unit length (PUL). The Telegrapher's equations in the time domain are

$$\frac{\partial}{\partial x} v(x, t) = -L \frac{\partial}{\partial t} i(x, t) - Ri(x, t) \tag{1a}$$

$$\frac{\partial}{\partial x} i(x, t) = -C \frac{\partial}{\partial t} v(x, t) - Gv(x, t). \tag{1b}$$

The transmission line stretches from 0 to d in the x-direction, where d is the length of the line. $v(x, t)$ is the voltage at point x at time t; $i(x, t)$ is the current at point x at time t.

Let

$$\xi = x + t/\sqrt{LC} \quad \text{and} \quad \eta = x - t/\sqrt{LC}.$$

The Telegrapher's equations in (1a) and (1b) can be transformed into the following form:

$$\frac{d}{d\eta} v(x, t) - Z_0 \frac{d}{d\eta} i(x, t) = -\frac{1}{2}\left(GZ_0 v(x, t) - Ri(x, t)\right)$$
$$\frac{d}{d\xi} v(x, t) + Z_0 \frac{d}{d\xi} i(x, t) = -\frac{1}{2}\left(GZ_0 v(x, t) + Ri(x, t)\right)$$

where $Z_0 = \sqrt{L/C}$ is the *characteristic impedance* of the transmission line. If the transmission line is *lossless* ($R = 0$ and $G = 0$) or

Manuscript received October 14, 1997. This work was supported in part by an Office of Naval Research Grant under a subcontract from Hughes Research Laboratory under Contract 300014-98-3-0010.

Q. Xu, Z.-F. Li, and J.-F. Mao are with the Department of Electronic Engineering, Shanghai Jao Tong University, Shanghai, China.

P. Mazumder is with the Department of Electrical Engineering, The University of Michigan at Ann Arbor, Ann Arbor, MI 48109-2122 USA.

Publisher Item Identifier S 0018-9480(00)00860-7.

if it is *undistorted line* ($LG = RC$), there exist the following simple recursive solutions:

$$v(0, t) - Z_0 i(0, t) = e^{-GZ_0 d}\left(v(d, t-\tau) - Z_0 i(d, t-\tau)\right) \quad (2a)$$

$$v(d, t) + Z_0 i(d, t) = e^{-GZ_0 d}\left(v(0, t-\tau) + Z_0 i(0, t-\tau)\right) \quad (2b)$$

where $\tau = d\sqrt{LC}$ is the delay time. In (2), by adding the boundary conditions and selecting a proper time step, the responses in the time domain can be obtained through recursive computation.

In such cases, the voltages and currents at two ends of the line are given by simple closed-form equations. However, for general lossy transmission lines with $LG \neq RC$, the simple relations no longer exist, but, a set of closed relations between the terminal responses can still be obtained by means of appropriate approximation.

III. New Model Using MMC

Assuming that the initial conditions are all zeros, there exist the following well-known relations for the general lossy transmission line in the frequency domain:

$$Y_0 V(0, s) - I(0, s) = \left[Y_0 V(d, s) - I(d, s)\right] e^{-\gamma d} \quad (3a)$$

$$Y_0 V(d, s) + I(d, s) = \left[Y_0 V(0, s) + I(0, s)\right] e^{-\gamma d} \quad (3b)$$

where $V(0, s)$ and $I(0, s)$ denote the Laplace-domain voltage and current at the near end of transmission line, respectively, and $V(d, s)$ and $I(d, s)$ are the counterparts at the far end. The term

$$\gamma = \gamma(s) = \sqrt{(sL + R)(sC + G)} \quad (4)$$

is the *propagation constant*, and

$$Y_0 = Y_0(s) = \sqrt{(sC + G)/(sL + R)} \quad (5)$$

is the *characteristic admittance* of the line.

For lossless lines with $R = G = 0$, it may be observed that $Y_0 = \sqrt{C/L}$ and $\gamma = s\sqrt{LC}$, and for undistorted lines with $LG = RC$, the propagation constant is given by $\gamma = s\sqrt{LC} + GZ_0$, while the characteristics admittance value remains the same as in the case of the lossless lines. In either case, (3) can be directly transformed into (2) through the inverse Laplace transformation. In the general case of $LG \neq RC$, if we define the following terms:

$$\alpha = G/C - R/L$$
$$\beta = R/L$$

and

$$u = \frac{\alpha}{s + \beta}$$

then it follows:

$$Y_0 = Y_{00}(1 + u)^{1/2} \quad (6)$$

where $Y_{00} = \sqrt{C/L}$. Obviously, α is a measurement of the departure from undistorted condition, and for an undistorted line, $\alpha = 0$. Under the definitions, (6) can be expanded into Maclaurin series in the following form:

$$\begin{aligned} Y_0 &= Y_{00} \sum_{n=0}^{\infty} c_n u^n \\ &= Y_{00}\left(1 + \frac{1}{2}u - \frac{1}{8}u^2 + \frac{1}{16}u^3 \cdots + c_n u^n + \cdots\right) \end{aligned} \quad (7)$$

where

$$c_n = \frac{1}{n!}\left[\frac{d^n}{du^n}\sqrt{1+u}\right]_{u=0}. \quad (8)$$

As (4) can also be represented by the form $\gamma = L(s + \beta)Y_0$, by substituting (7) in to it, we obtain

$$\begin{aligned} \gamma &= Y_{00} L(s+\beta) \sum_{n=0}^{\infty} c_n u^n \\ &= s\sqrt{LC} + Y_{00} L\beta + Y_{00} L(s+\beta) \sum_{n=1}^{\infty} c_n u^n. \end{aligned} \quad (9)$$

According to (7) and (9), (3) becomes

$$\begin{aligned} &V(0, s)Y_{00} \sum_{n=0}^{\infty} c_n u^n - I(0, s) \\ &\quad = \left[V(d, s)Y_{00} \sum_{n=0}^{\infty} c_n u^n - I(d, s)\right] e^{-s\tau} Q(s) \end{aligned} \quad (10a)$$

$$\begin{aligned} &V(d, s)Y_{00} \sum_{n=0}^{\infty} c_n u^n + I(d, s) \\ &\quad = \left[V(0, s)Y_{00} \sum_{n=0}^{\infty} c_n u^n + I(0, s)\right] e^{-s\tau} Q(s) \end{aligned} \quad (10b)$$

where

$$Q(s) = \exp\left(-d\left(Y_{00} L\beta + Y_{00} L(s+\beta) \sum_{n=1}^{\infty} c_n u^n\right)\right). \quad (11)$$

Let

$$I_1(0, s) = V(0, s)Y_{00} u \quad (12a)$$

$$I_1(d, s) = V(d, s)Y_{00} u \quad (12b)$$

$$I_{j+1}(0, s) = V(0, s)Y_{00} u^{j+1} = I_j(0, s)u \quad (13a)$$

$$I_{j+1}(d, s) = V(d, s)Y_{00} u^{j+1} = I_j(d, s)u, \qquad j = 1, 2, \cdots. \quad (13b)$$

If we take the first $N + 1$ items in (7) and then take the inverse Laplace transform of (10)–(13), the following equations in the time domain can be obtained:

$$\begin{aligned} &Y_{00} v(0, t) - i(0, t) + \sum_{n=1}^{N} c_n i_n(0, t) \\ &\quad = \left[Y_{00} v(d, t-\tau) - i(d, t-\tau) + \sum_{n=1}^{N} c_n i_n(d, t-\tau)\right] \\ &\quad\quad * L^{-1}(Q(s)) \end{aligned} \quad (14a)$$

$$\begin{aligned} &Y_{00} v(d, t) + i(d, t) + \sum_{n=1}^{N} c_n i_n(0, t) \\ &\quad = \left[Y_{00} v(0, t-\tau) + i(0, t-\tau) + \sum_{n=1}^{N} c_n i_n(0, t-\tau)\right] \\ &\quad\quad * L^{-1}(Q(s)) \end{aligned} \quad (14b)$$

$$\begin{aligned} &\alpha Y_{00} v(0, t) \\ &\quad = \beta i_1(0, t) + \frac{d}{dt} i_1(0, t) \end{aligned} \quad (15a)$$

$$\alpha Y_{00} v(d, t) = \beta i_1(d, t) + \frac{d}{dt} i_1(d, t) \tag{15b}$$

$$\alpha i_j(0, t) = \beta i_{j+1}(0, t) + \frac{d}{dt} i_{j+1}(0, t) \tag{16a}$$

$$\alpha i_j(d, t) = \beta i_{j+1}(d, t) + \frac{d}{dt} i_{j+1}(d, t), \qquad j = 1, 2, \cdots, N-1 \tag{16b}$$

where $L^{-1}(Q(s))$ is the inverse Laplace transform of $Q(s)$ and * is the operator of convolution integration.

The above equations represent the solution of the MMC. In comparison with the normal characteristic method for lossless and undistorted conditions, the so-called additional current terms $I_1, I_2, \cdots, I_N$ and $i_1, i_2, \cdots, i_N$ are added in the formulas. However, the recursive relation of voltages and currents between two ends of the line still holds.

Let us focus on how to get the item $L^{-1}(Q(s))$. $Q(s)$ is matched to a Padé approximation with both the numerator polynomial and denominator polynomial of the same degree n; i.e.,

$$Q(s) = \frac{a_n s^n + a_{n-1} s^{n-1} + \cdots + a_1 s + 1}{b_n s^n + b_{n-1} s^{n-1} + \cdots + b_1 s + 1} = \frac{a_n}{b_n}\left(1 + \sum_{i=1}^{n} \frac{q_i}{s - p_i}\right) \tag{17}$$

so $Q(s)$ can be transformed into the time domain [5].

The complexity for direct computation of (14) is considerable because of the convolution integration. It is also found that the single-point Padé approximation in (17) cannot guarantee the stability. However, if we further simplify the approximation of (7), the instability will be avoided, and the computation will be very efficient.

IV. The First-Order Approximation of the MMC Model

If only the first two items are taken in (7), i.e., $N = 1$, the simplified macromodel can be obtained, which is called the *first-order* model. In such a case, the only fixed pole is $s = -\beta$ and no right half-plane poles occur, while the process of (17) is bypassed. Accordingly, the following equations in the time domain are obtained:

$$Y_{00} v(0, t) - i(0, t) + c_1 i_1(0, t) = \Big[Y_{00} v(d, t-\tau) - i(d, t-\tau) + c_1 i_1(d, t-\tau)\Big] Q_0 \tag{18a}$$

$$Y_{00} v(d, t) + i(d, t) + c_1 i_1(0, t) = \Big[Y_{00} v(0, t-\tau) + i(0, t-\tau) + c_1 i_1(0, t-\tau)\Big] Q_0 \tag{18b}$$

and

$$\alpha Y_{00} v(0, t) = \beta i_1(0, t) + \frac{d}{dt} i_1(0, t) \tag{19a}$$

$$\alpha Y_{00} v(d, t) = \beta i_1(d, t) + \frac{d}{dt} i_1(d, t) \tag{19b}$$

where

$$Q_0 = \exp\Big[-Y_{00} L d(\beta + \alpha/2)\Big].$$

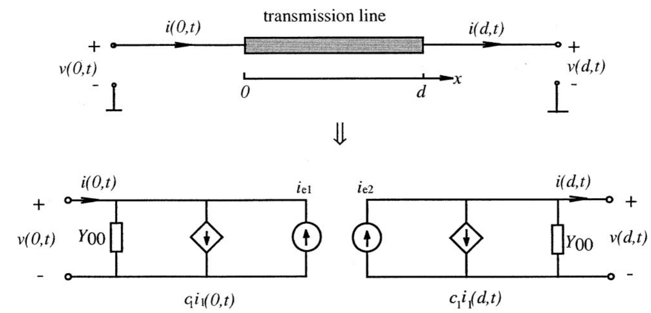

Fig. 1. Transmission line characteristics model.

Equations (18) and (19) represent the first-order approximation of the MMC model. There is only one additional current term i_1 in the formulas. The simplified model is illustrated in Fig. 1, where

$$i_{e1} = \Big[Y_{00} v(d, t-\tau) - i(d, t-\tau) + c_1 i_1(d, t-\tau)\Big] Q_0$$

$$i_{e2} = \Big[Y_{00} v(0, t-\tau) + i(0, t-\tau) + c_1 i_1(0, t-\tau)\Big] Q_0.$$

In the process of recursive operations, a queue of memory is needed to store the previous voltage and current values, and the data preceding $t - \tau$ can be deleted from the queue. In fact, high accuracy can be obtained when the simplified macromodel is employed, thus the algorithm remains efficient for general uniform lossy transmission lines.

Next, we show that the first-order model can satisfy the required accuracy. The errors of (18) and (19) occur due to the truncation error of the Maclaurin series in (7). In the extreme case, when $G = 0$, the error of Y_0, $\mathrm{Err}(Y_0)$, is given by

$$\mathrm{Err}(Y_0) = Y_{00} \sum_{n=2}^{\infty} c_n u^n = \sqrt{\frac{C}{L}}\left(-\frac{1}{8}\left(\frac{R/L}{s + R/L}\right)^2 - \frac{1}{16}\left(\frac{R/L}{s+R/L}\right)^3 \cdots\right).$$

The PUL parameters L and C usually vary within a small range, and are determined by the material and geometry of transmission lines, while R is generally determined by the size of the cross section of an interconnection conductor. For any parameter s, $\mathrm{Err}(Y_0)$ is related to the parameter R and

$$\lim_{R \to 0} \mathrm{Err}(Y_0) = 0.$$

For lossless lines with $R = 0$, we find that $\mathrm{Err}(Y_0) = 0$. This case is shown by (2).

As the errors in (18) and (19) are owing to only $\mathrm{Err}(Y_0)$, it is shown that the smaller the value of R is, the less the value of the error will occur, i.e., $\mathrm{Err}(Y_0)$ will be smaller. For interconnects on MCM's, the typical value of characteristic impedance $Z_0 = 1/Y_0$ varies from 50–100 Ω. Take Fig. 1 as an example. Let us assume that the left-hand-side end of the transmission line is connected to a voltage source having a source resistance of 50 Ω, and that a load resistance of 50 Ω terminates the right end of the line. If the cross section of conductor is 25 μm × 8 μm, and the resistivity of material is about $\rho = 2 \times 10^{-8}$ Ω·m, then the PUL parameter R is about 100 Ω·m. Let us assume that the parameters of transmission line are $L = 360$ nH/m, $C = 100$ pF/m, $d = 0.08$ m, $G = 0$, and the value of R varies as 100, 200, 300, and 500 Ω/m, respectively. Let the applied voltage be a pulse having 0.5-ns rise and fall times and 3-ns width.

Fig. 2 shows the results of this method and those of the FFT method. Fig. 2 shows that the results from this approach are in accordance with those from the FFT method when R is not too large. The parameter R

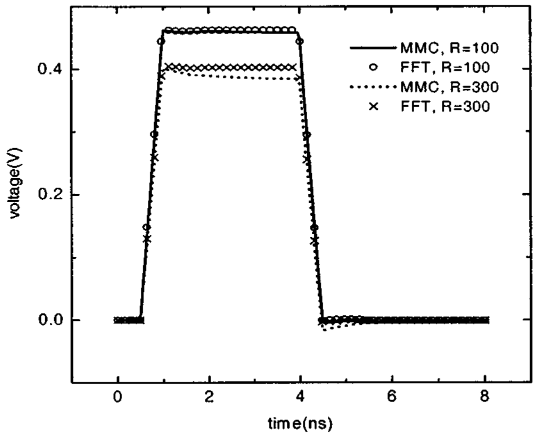

Fig. 2. Results for various resistances.

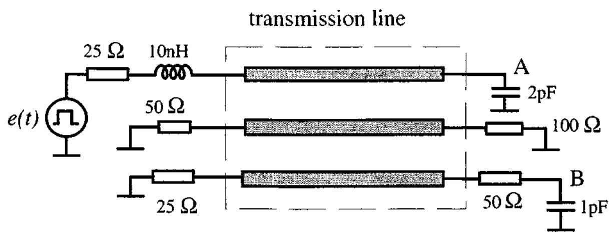

Fig. 3. Example circuit.

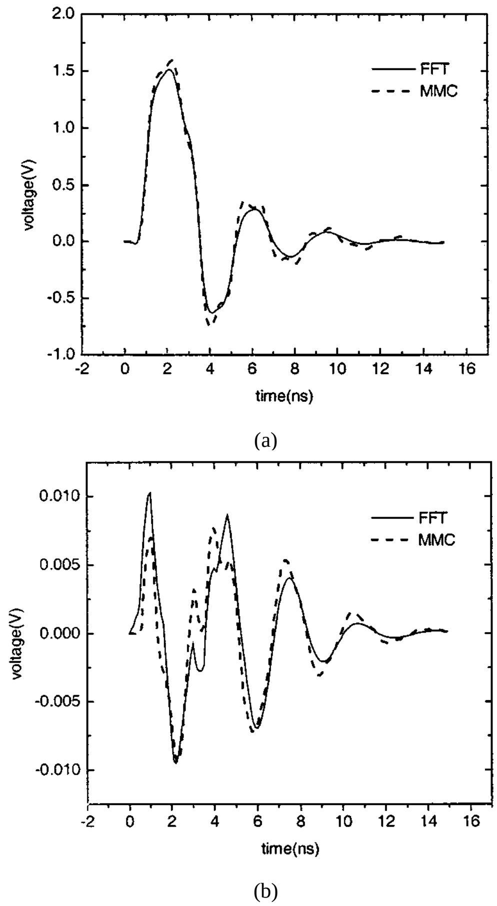

Fig. 4. Results for example circuit. (a) Waveform of A. (b) Waveform of B.

can vary to a large extent. For example, R can be as high as 300 Ω/m, and the results of this method are still in accordance with those of the FFT method.

For multiconductor coupled lines, the PUL parameters L, C, R, and G become matrix parameters and $v(x, t)$ and $i(x, t)$ are represented by vectors accordingly. As long as such Telegrapher's equation can be decoupled into M modes, each of them is similar to a single transmission line; therefore, they can be handled in similar manners.

If $\boldsymbol{L}$, $\boldsymbol{C}$, $\boldsymbol{R}$, and $\boldsymbol{G}$ are Toeplitz matrices, the method can directly apply to this case. There is another case to which the method can be applied easily. In this case, the dielectric media is homogeneous, and $\boldsymbol{R}$ is a diagonal matrix, while all the elements of matrix $\boldsymbol{G}$ are zero [9]. In reality, this situation represents that of the MCM. The method has its own advantages, but it also has its limitations. The method is highly efficient only if the coupled lines can be decoupled. Otherwise, the numerical method of characteristic should be used [11].

V. Numerical Results

Let us assume that a circuit is composed of lossy-coupled transmission line, as shown in Fig. 3. The length of the line is 0.1 m. Other parameters are

$$\boldsymbol{L} = \begin{bmatrix} 494.6 & 63.3 & 0 \\ 63.3 & 494.6 & 63.3 \\ 0 & 63.3 & 494.6 \end{bmatrix} \text{ nH/m}$$

$$\boldsymbol{C} = \begin{bmatrix} 62.8 & -4.9 & 0 \\ -4.9 & 62.8 & 4.9 \\ 0 & -4.9 & 62.8 \end{bmatrix} \text{ pF/m}$$

$$\boldsymbol{R} = \begin{bmatrix} 50 & 10 & 0 \\ 10 & 50 & 10 \\ 0 & 10 & 50 \end{bmatrix} \Omega/\text{m}$$

$$\boldsymbol{G} = \begin{bmatrix} 0 & 0 & 0 \\ 0 & 0 & 0 \\ 0 & 0 & 0 \end{bmatrix}.$$

The applied voltage is a pulse of width 2 ns and amplitude 1 V having a 0.5 ns rise/fall time. The results are shown in Fig. 4(a) and (b), along with the results of the FFT. In Fig. 4(b), it can be seen that the FFT is not as accurate as the MMC in evaluating the delay time.

VI. Conclusions

In this paper, a new time-domain model of lossy transmission lines has been proposed using the MMC, and its first-order approximation has been applied to simulate high-speed single and multiple interconnects in the time-domain. The proposed MMC model is based on the classical MC, and it uses simple recursive algorithm. The algorithm of the first-order approximation of the model reduces the computational complexity of interconnect simulation. Taking the appropriate time step, the transient responses in the time domain can be obtained simply through recursive operations. In the MMC model, only the quantities at two ends of the transmission lines are utilized in the calculation, thereby requiring considerably less storage area for the computation. Since the MMC does not employ any convolution, the algorithm of the simplified model retains high efficiency as well as that it guarantees absolute stability. Numerical experiments confirm that the model of first-order approximation can, in general, yield results with high accuracy.

References

[1] W. W. M. Dai, "Guest editor's introduction," *IEEE Trans. Circuits Syst. I*, vol. 39, pp. 857–860, Nov. 1992.

[2] A. R. Djordjevic, T. K. Sarkar, and R. F. Harrington, "Time-domain response of multiconductor transmission lines," *Proc. IEEE*, vol. 75, pp. 743–764, June 1987.

[3] J. E. Schutt-Aine and R. Mittra, "Scattering parameter transient analysis of transmission lines loaded with nonlinear termination," *IEEE Trans. Circuits Syst. I*, vol. 36, pp. 529–536, Apr. 1988.

[4] T. Pillage and R. A. Rohrer, "Asymptotic waveform evaluation for timing analysis," *IEEE Trans. Computer-Aided Design*, vol. 9, pp. 352–377, Apr. 1990.

[5] S. Lin and E. S. Kuh, "Transient simulation of lossy interconnects based on the recursive convolution formulation," *IEEE Trans. Circuits Syst. I*, vol. 39, pp. 879–892, Nov. 1992.

[6] T. K. Tang and M. Nakhla, "Analysis of high-speed VLSI interconnects using the asymptotic waveform evaluation technique," *IEEE Trans. Computer-Aided Design*, vol. 11, pp. 341–352, Mar. 1992.

[7] E. Chiprout and M. Nakhla, "Analysis of interconnect networks using complex frequency hopping," *IEEE Trans. Computer-Aided Design*, vol. 14, pp. 186–199, Feb. 1995.

[8] A. Odabasioglu, M. Celik, and L. T. Pillage, "PRIMA: Passive reduced-order interconnect macromodeling algorithm," in *Proc. ICCAD*, Nov. 1997, pp. 58–65.

[9] F.-Y. Chang, "The generalized method of characteristics for waveform relaxation analysis of lossy coupled transmission lines," *IEEE Trans. Microwave Theory Tech.*, vol. 37, pp. 2028–2038, Dec. 1989.

[10] J.-F. Mao and Z.-F. Li, "Analysis of the time response of transmission lines with frequency-dependent losses by the method of convolution characteristic," *IEEE Trans. Microwave Theory Tech.*, vol. 40, pp. 637–645, Apr. 1992.

[11] J.-F. Mao and E. S. Kuh, "Fast simulation and sensitivity analysis of lossy transmission lines by the method of characteristics," *IEEE Trans. Circuits Syst. I*, vol. 44, pp. 391–400, May 1997.